



universität  
wien

# MASTERARBEIT / MASTER'S THESIS

Titel der Masterarbeit / Title of the Master's thesis

**„Analysis of Crackling Noise in porous materials  
by strain drop measurements“**

verfasst von / submitted by

Sabine Friedericke Puchberger, Bsc

angestrebter akademischer Grad / in partial fulfilment of the requirements for the degree of

Master of Science (Msc)

Wien, 2016 / Vienna, 2016

Studienkennzahl lt. Studienblatt / degree program  
code as it appears on the student record sheet: A 066 876

Studienrichtung lt. Studienblatt / degree program as  
it appears on the student record sheet: Physik

Betreut von / Supervisor:

ao. Univ.-Prof. Mag. Dr. Wilfried Schranz



# Eidesstaatliche Erklärung

Hiermit versichere ich,

dass ich die vorliegende Masterarbeit selbstständig verfasst, andere als die angegebenen Quellen und Hilfsmittel nicht benutzt und mich auch sonst keiner unerlaubter Hilfe bedient habe,

dass ich dieses Masterarbeitsthema bisher weder im In- noch im Ausland in irgendeiner Form als Prüfungsarbeit vorgelegt habe

und dass diese Arbeit mit der vom Begutachter beurteilten Arbeit vollständig übereinstimmt.

Sabine Puchberger, Februar 2016



# Acknowledgements

First and foremost I want to express my gratitude to Wilfried Schranz, being the kind and considerate professor he is, for giving me the opportunity to work on this thesis and for his continuous support.

As well, I would like to thank Viktor Soprunyuk who always took the time to answer my questions and showed me how to use the equipment and how to work on this project.

During the years of my studies I gained several friends and met even more lovely people with whom I share happy memories. In particular, I would like to mention Marianne Pietschnig and Dominik Ballek, who are both continuously supporting and encouraging me.

Beyond all, I devote my deep gratefulness to my family, hence, without them this journey would not have been possible. Especially, I thank my brother Christian who inspires me in so many ways.

Last but not least, I want to thank my dear friend Johanna Auzinger, who took the time revising my thesis and who won the battle against plenty of grammatical and spelling errors.



# Contents

<b>1</b>	<b>Introduction</b>	<b>9</b>
<b>2</b>	<b>Physical Background</b>	<b>11</b>
2.1	Crackling noise . . . . .	11
2.1.1	Power-law behavior and scale invariance . . . . .	12
2.1.2	Universality . . . . .	14
2.1.3	Complex systems and self-organized criticality . . . . .	15
2.2	Omori's law . . . . .	16
2.3	Values of critical exponents predicted by mean-field theory . . . . .	17
<b>3</b>	<b>Preceding work on crackling in porous materials</b>	<b>21</b>
3.1	Crackling noise in porous Vycor . . . . .	22
3.2	Statistical similarities between compression of porous Vycor and earthquakes	24
3.3	Crackling noise in synthetic and natural SiO <sub>2</sub> -based materials . . . . .	27
<b>4</b>	<b>Laboratory equipment</b>	<b>31</b>
4.1	Measurement tools . . . . .	31
4.1.1	IsoMet <sup>TM</sup> Low Speed Saw . . . . .	31
4.1.2	Dynamic Mechanical Analyzer . . . . .	31
4.2	Measurement & data evaluation software . . . . .	35

<b>5</b>	<b>Samples and sample preparation</b>	<b>37</b>
5.1	Samples . . . . .	37
5.1.1	Shale . . . . .	37
5.1.2	Vycor . . . . .	38
5.1.3	Gelsil . . . . .	39
5.2	Sample preparation . . . . .	42
<b>6</b>	<b>Measurement procedure</b>	<b>43</b>
6.1	Shale . . . . .	43
6.1.1	Samples and measurement set-ups . . . . .	43
6.1.2	Shale measurements . . . . .	45
6.2	Vycor . . . . .	50
6.2.1	Samples and measurement set-up . . . . .	50
6.2.2	Vycor measurements . . . . .	51
6.3	Gelsil . . . . .	53
6.3.1	Samples and measurement set-up . . . . .	53
6.3.2	Gelsil measurements . . . . .	54
<b>7</b>	<b>Analysis of data</b>	<b>61</b>
7.1	First evaluation method - 'searching for power-laws in the wrong region' . . . . .	61
7.2	New evaluation method - Logarithmic binning transformed to linear . . . . .	65
<b>8</b>	<b>Acoustic emission data for Vycor 7.5nm</b>	<b>81</b>
<b>9</b>	<b>Conclusion</b>	<b>85</b>

# 1 Introduction

This master thesis investigates the concept of crackling in nanoporous materials.

In this case, crackling refers to a jerky response of a system to changing external conditions for example a driving force, a temperature or an electric or magnetic field. The disturbance of the system through external forces results in impulsive events (avalanches) of a variety of sizes. Crackling events can occur in different systems: crumpling pieces of paper, magnetizing domains via jumps in magnetization (Barkhausen effect) and in tectonic plate movement resulting in earthquakes, and other similar phenomena. It has been discovered that many of those systems exhibiting crackling events show similar power-law statistics [26].

In the case of porous materials crackling can be observed when the material is compressed and avalanches occur due to the correlated nanometer-scaled pore breaking. As a result, the sample deforms not continuously but in little jerks [4].

Recent studies (e.g. [4], [27], [23]) on selected porous materials have shown that this behavior can be analyzed by applying a compressive force on the sample and simultaneously measuring the acoustic emission. An analysis of the energy distribution of the acoustic emission activities revealed power-law characteristics with critical exponents stable over several orders of magnitude similar to earthquake statistics. Acoustic emission is a very sensitive technique to study crackling noise that enables the recording of acoustic waves resulting from sample strain in the range of MHz. Acoustic emission is successful in measuring collapses in porous materials and some martensite transformations but this method faces its limits of applicability when confronted with micron-scale samples, which are important for nano-technology applications. Therefore, it has become of increasing importance to develop alternative methods that compensate the drawbacks of acoustic emission

## 1 Introduction

while having a high dynamical range [30].

The main task during the work on this thesis was to analyse and introduce a new method for studying crackling in porous materials. The most important questions were concerned with finding out whether similar power-law behaviors of the avalanche statistics (like the energy distribution) as in acoustic emission experiments can be obtained by measuring the jerky evolution of the sample height. From the height changes of the sample, the square of the time derivatives of the sample height (which are often referred to as squared drop velocities) can be calculated. These squared drop velocities are assumed to be proportional to the energy that is released during the collapsing of pores under compression. Then, the calculated squared drop velocity distributions are compared to acoustic emission energy distributions via fitting power-laws yielding estimations of critical exponents.

In the following, the resulting power-law exponents from these calculated squared drop velocity distributions can be compared to previous studies on the same porous materials. Additionally, other characteristic distributions and their exponents are investigated and compared to references, including the exponent of the Omori's law for earthquakes, which concerns the rate of aftershocks. The investigations on crackling also reveal whether the acoustic emission activity can indeed be assumed to be the energy released during pore collapsing.

The measurements were performed using a Dynamic mechanical analyzer (DMA), which was responsible for both applying the compressive force and measuring the sample deformation. Compressive stress was applied slowly with rates of about  $0.1mN/s - 10mN/s$ . The samples selected were on the one hand Gelsil and Vycor, both  $SiO_2$ -based synthetic materials, which have been studied previously with acoustic emission and, on the other hand, Shale which is a natural porous sedimentary rock.

The measurement techniques of acoustic emission and strain drops in experiments, which are done under slow compression, are of great interest for studying mechanical failure in porous materials. In addition, strain drop experiments with the DMA have great potential for becoming a tool to study earthquake dynamics in micron-sized materials in the laboratory, also at different conditions, like at high temperatures [30].

## 2 Physical Background

### 2.1 Crackling noise

Crackling noise is a phenomenon observed in many different systems which initially do not appear to have anything in common, like the magnetization of magnetic materials at external fields, plastic deformation in crystals, the compression of porous materials, earthquakes and even decision-making processes and crumpling of pieces of paper [26].

The concept of crackling is often used to refer to a jerky behavior with events of a multitude of sizes as response of such a system to some external condition, for example an applied force [26], [29].

In the case of the magnetization of magnetic materials, this means that the material magnetizes at applied external magnetic field not continuously but in little jumps or jerks, this behavior is called Barkausen noise and can be explained by the flip-over of magnetic domains. As the material enters an external magnetic field, the domains rearrange (in case of e.g. an ferromagnetic material) in a way so that the field is increased, hence the domains orientate themselves parallel to the external field. (In case of a ferromagnet each domain prefers to point in the same direction of its neighbor domains and, in this way, the ferromagnet gets magnetized.) Depending on the amount of disorder present in the ferromagnetic material, this flipping process occurs in several varieties: If the disorder is small the flipping of domains occurs in form of one large avalanche spanning over the whole material. However, if the disorder is large, many small flipping events occur as the domains react independently from one another. Somewhere inbetween these two extremes, at the critical disorder  $R_c$ , avalanches of these spin-flips occur in a multitude of sizes [29].

## 2 Physical Background

When it comes to plastic deformation in crystals, crackling is present in form of displacement jumps. This behaviour shows up in the stress-strain-curves as 'strain jumps' at applied stress [26].

In porous materials the crackling is due to a collapsing of pores and cavities [26] and in case of earthquakes the crackling results from tectonic plate movement [29].

### 2.1.1 Power-law behavior and scale invariance

Another example of a crackling system is the model of a sandpile from Bak, Tang, Wiesenfeld [3], [29]. In this model, sand is added grain after grain until the sandpile has increased enough to reach a critical height or critical point. Further adding of grains may now result in avalanches of sand. Once having reached this critical point, one more added grain may cause a huge avalanche, medium-sized avalanches or just a single neighbouring grain to fall down along the slope [3], [2]. In other words, this model acts the same at the critical point as ferromagnetic materials magnetize in an applied external field, as explained above.

Avalanches of sand grains can occur in a wide range of sizes. This phenomenon can also be seen in earthquakes, where events occur in different magnitudes [29]. Gutenberg and Richter came up with the idea of describing the magnitude-frequency relationship of earthquakes with a power law, called the Gutenberg-Richter law [15]:

$$\log N(M) = a - bM \quad (2.1)$$

here,  $a$  and  $b$  are constants,  $N$  denotes the number of occurring earthquakes of magnitude  $M$  in a certain region [15].

In figure 2.1 one can see a histogram of the number of earthquakes as function of their magnitude [28]. It can be seen that earthquakes appear on different size scales and weaker earthquakes occur much less frequently than very powerful quakes of high magnitude.

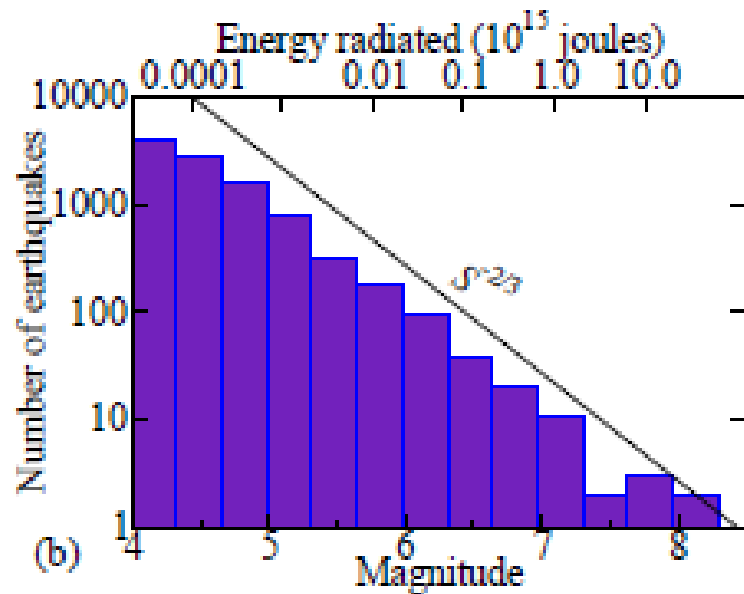


Figure 2.1: Histogram of the number of earthquakes in 1995 as a function of their magnitude [28]

The number of avalanches of a certain size occurring in the sandpile model, magnetic materials and earthquakes, that have been described so far, show all the same power law behavior. It can be written in the form of [28]:

$$D(s) = s^{-\tau} \quad (2.2)$$

This power law is valid over many different size scales [28]. However, the size scale one of these systems is observed with does not matter for the occurring events, which is why this behavior is called a scale-invariant behavior [29].

This behavior can be visualized with the help of the sandpile model: once the critical height is reached, e.g. for a little ant and a much larger mouse living in the sandpile, their 'sandpile world' basically looks the same, as the size of the occurring avalanches does not depend on the size scale (assuming, of course, both the ant and the mouse are just watching their sandpile without having any influence on the dynamics).

## 2 Physical Background

So, apparently, the behaviors of these systems have a common feature, which is independent of both the macroscopic and microscopic details of the systems [29]. Therefore, a new term is introduced in the study of these non-linear, dynamic systems which is called 'universality' [29], [28].

### 2.1.2 Universality

Universality is a concept known from continuous phase transitions.<sup>1</sup> One example shall be continuous phase transitions at the critical point. The critical point could be for example the Curie point  $T = T_C$  at which a ferromagnetic material loses its ferromagnetic properties upon a temperature increase. Another example of a critical point is the starting point of the coexistence region of a liquid and a vapor phase of a material. Corresponding critical parameters are the critical temperature, pressure and density [8].

However, the interesting feature is that, in approaching these critical points, different systems show the same behavior, which is called universality [28]. When approaching a critical point, certain physical quantities either diverge to infinity, as e.g. the correlation length of spin-spin correlations or susceptibilities, or converge to zero, as e.g. the macroscopic magnetic moment [8].

When describing critical phenomena it has proven useful to introduce some 'order parameters' (according to the Landau-Theory of phase transitions) which could be the density difference of the vapor and liquid phase near the critical point, or the spontaneous magnetization of the ferromagnetic phase. Upon approaching the critical point, these order parameters converge to zero in the form of [18]:

$$\Theta \propto |T - T_c|^\beta \quad (2.3)$$

$\Theta$  denotes an order parameter,  $T_c$  the critical temperature and the exponent  $\beta$  is the 'critical exponent' which is of extreme importance for a large group of phase transitions [18].

---

<sup>1</sup>Continuous phase transitions are distinguished from discontinuous (or first order phase transitions) in which the first derivative of some thermodynamical potential with respect to some thermodynamic variable shows a discontinuity. Continuous transitions on the other hand would not show a discontinuity in the first derivative, but at some higher order of derivative [8].

The critical exponents of such order parameters are universal (according to Landau-Theory) which means that their value is independent from details of the interaction, but only dependent on more general characteristics, as for example the dimension of the system and the range of interaction [18].

Other systems showing the same critical exponents are grouped into the same 'universality class' and, hence, show the same long length scale behavior. In order to study universality, renormalization group methods are used [28], [29]. Scale invariance near criticality is the reason why crackling noise is being studied while occurring in the fracture of materials (especially porous materials) and why the results (critical exponents) can be compared with some seemingly completely different systems.

As power-law characteristics near the critical points can be found in continuous phase transitions, scale invariance appears in these phenomena as well. Studies have proved that many of the crackling noise systems can be studied as critical points and therefore as some sort of a phase transition. (Which in turn is the reason why crackling can be analyzed using renormalization group and scaling methods - tools usually employed for studying continuous phase transitions.<sup>2</sup>) [28]

Therefore, it can be deduced that there is some sort of connection between crackling noise and phase transitions. It might seem rather farfetched to regard earthquakes as some sort of phase transition, however, it can be explained in a more closer investigation of the sandpile model.

### 2.1.3 Complex systems and self-organized criticality

As discussed above, the sandpile model arises from the idea of adding grains of sand one after another to a pile of sand. After some time, a critical height is reached and adding one additional grain may cause an avalanche of sand, which can be of any size within a broad range of sizes. If the critical height is not yet reached, added grains will not cause huge avalanches, but tend to stick where they land or close by, and their motion is described by their physical properties. As the critical height is reached, however, something changes:

---

<sup>2</sup>For further information on renormalization group and scaling methods, see Sethna, 2011 [28]

## 2 Physical Background

avalanches can be of any size and the behavior of the system cannot be explained with the behavior of single grains any more. What has actually happened is that the system transformed to a complex system whose properties can only be explained taking into account the sand pile as a whole. The occurrence of such a complex system is linked to self-organized criticality. Regarding the sandpile model it means that the sandpile has organized itself and evolved automatically into a critical state [2].

Self organized criticality is defined as a behavior of a system that has an attractor of some kind leading it to evolve into a state where scale-invariant events occur with power law behavior of the size distribution of these events [11].

When taking into account earthquakes, some similarities to the sandpile model can be found: Tectonic plates are moving towards each other and have an impact on one another in form of pressures which result in instabilities and quakes. The number and magnitude (or energy) of earthquakes occurring as result of tectonic plate interaction is described with a power-law (as mentioned before according to the Gutenberg-Richter law). Therefore, earthquakes show a scale-invariant, universal behavior like the avalanches of the sandpile model, and because of their power law behavior earthquakes can be seen as self-organized critical systems [1].

In his work "How nature works: the science of self-organized criticality" Per Bak explains how Earth has organized itself into a critical state by tectonic plate movements, earthquakes, and volcanic eruptions in the course of time (over hundreds of million years). As released earthquakes can be of any size and follow the Gutenberg-Richter law, evidence is given to these assumptions [2].

### 2.2 Omori's law

Omori discovered 1894 that after a main earthquake event, several smaller earthquakes (aftershocks) occur and their number decreases with time in form of a power law. Omori found this formula via studying aftershock frequencies (half-day and monthly frequencies) of earthquakes in Japan. One of the aftershock sequences he studied was following the 1891

Mino-Owari earthquake in central Japan [31].

This so called Omori's law is given by [15]:

$$n(t) = K \cdot (t + c)^{-1} \quad (2.4)$$

$n(t)$  denotes the number of aftershocks per unit time,  $K$  and  $c$  being constants [15].

A modified version of this formula was developed by Hirano (1924) who studied daily frequencies of aftershocks near Tokyo since the great Kanto earthquake in September 1923 [31]:

$$n(t) = K \cdot (t + c)^{-p} \quad (2.5)$$

The exponent  $p$  that is usually close to 1 [15].

## 2.3 Values of critical exponents predicted by mean-field theory

The mean-field theory (MFT)<sup>3</sup> is used for analyzing slip avalanches in crackling systems theoretically. It derives scaling behaviors of these slip avalanches, their statistical distributions and predicts values for the critical exponents. (MFT also predicts certain relations between the critical exponents.) Using this theory various distributions can be analyzed, not only the slip-size distribution, but also others like the avalanche duration distribution, the energy distribution and the slip-velocity distribution [26].

Salje et al. [26] estimated some values for critical exponents for different distributions according to MFT, see selected distributions including their exponents in tabular 2.1.

---

<sup>3</sup>MFT is used to study phase transitions and can be regarded as approximation for the thermodynamic properties of a system. In this theory order parameters are assumed to be spatially constant and despite this assumption MFT is able to predict certain quantitative properties of phase transitions correctly (in high spatial dimensions), e.g. critical exponents [5].

## 2 Physical Background

The Energy distribution is calculated from integration of the drop velocity squared values  $v(t)^2$  over corresponding peaks [30]:

$$E \propto \frac{1}{T} \cdot \int_T v(t)^2 dt \quad (2.6)$$

T denotes the time period of a slip event. The corresponding energy distribution  $D(E) \sim E^{-\epsilon}$  has an exponent of 4/3 according to MFT, see second line of tabular 2.1 [26].

In case the energy is defined differently, e.g. in some acoustic emission experiments<sup>4</sup>, the scaling behavior of the distribution changes. When considering only the maximum drop velocity squared values  $v_m^2$ , which are the values exactly at each peak (i.e. the largest values during an avalanche), the energy is defined as  $E_m \sim v_m^2$  and the distribution can be written as  $D(E_m) \sim (v_m^2)^{-\epsilon'}$  [26]. The exponent values for such distributions are displayed in the fourth and fifth line in table 2.1.

Table 2.1: Selected exponent values predicted by MFT [26]

Distribution	Formula	Exponent	Exponent value
Size distribution	$D(S) \sim S^{-\tau}$	$\tau$	1.5
Energy distribution	$D(E) \sim E^{-\epsilon}$	$\epsilon$	1.33
Stress-integrated energy distribution	$D_{int}(E) \sim E^{-\epsilon_{int}}$	$\epsilon_{int}$	1.67
Stress-integrated maximum velocity squared distribution	$D_{int}(v_m^2) \sim (v_m^2)^{\epsilon'_{int}}$	$(\epsilon')_{int}$	2.0
Maximum velocity squared distribution	$D(v_m^2) \sim (v_m^2)^{-\epsilon'}$	$\epsilon'$	1.5

Stress-integrated exponents stem from experiments where the external stress is increased gradually until failure, resulting in an emergence of avalanches during compression [19].

<sup>4</sup>In the DMA measurements the energy is defined with the maximum drop velocity squared values.

### 2.3 Values of critical exponents predicted by mean-field theory

The exponent  $\mu$  of the maximum velocity distribution  $D(v_m) \sim v_m^{-\mu}$  is related to the exponent of the maximum velocity squared distribution  $\epsilon'$ . This relation can be calculated with the identity:

$$D(v_m^2)d(v_m^2) = D(v_m)d(v_m) \quad (2.7)$$

Equation 2.7 arises from the fact that the integral of the probability density (i.e. the probability) is invariant under variable transformation of the probability density. This equation can be rewritten with the formulas for the distributions (tabular 2.1) to:

$$(v_m^2)^{-\epsilon'} d(v_m^2) = v_m^{-\mu} d(v_m) \quad (2.8)$$

$$2 \cdot (v_m^2)^{-\epsilon'} v_m d(v_m) = v_m^{-\mu} d(v_m) \quad (2.9)$$

$$2 \cdot (v_m)^{-2\epsilon'+1} = v_m^{-\mu} \quad (2.10)$$

Thus, the relation of the exponents  $\mu$  and  $\epsilon'$  is given in a form:

$$\mu = 2\epsilon' - 1 \quad (2.11)$$

Assuming  $\epsilon'$  to be 1.5 according to MFT, tabular 2.1, the exponent of the maximum velocity distribution is  $\mu = 2$ .



# 3 Preceding work on crackling in porous materials

Crackling noise has been studied and analyzed in different systems and fields, for example in magnetic materials (Barkhausen noise), martensitic phase transitions, plastically deformed small crystals, decision-making processes, stock market fluctuations and many more [26], [29]. In this thesis, the focus has been placed on studying crackling noise in porous materials. Porous materials show a crackling behavior upon application of an external force. They get compressed slowly when pores are collapsing due to the increasing stress with a jerk-like behavior typical for crackling systems.

As explained in the previous section, different crackling systems can share the same statistical characteristics and, hence, be part of the same universality class. A comparison can be made of these different systems with the help of critical exponents of corresponding power laws. In this manner, by studying one system that is part of a universality class, it is possible to get information about other systems of the same universality class. Knowledge obtained for such a studied system can then be applied to other systems of the same universality class and, hence, predictions can be made even for systems not directly measured themselves [26].

Understanding how porous materials respond to an external stress is an interesting research topic, as the failure mechanisms in these materials play an important role in Mining, building industry and geology. In the context of Mining, porosity of minerals might cause severe accidents in form of landslides or collapse of mining shafts. Historic buildings may be damaged because their porous building stones are subject to external forces [27].

### 3 Preceding work on crackling in porous materials

The crackling in porous materials is due to the collapsing of pores and cavities in the samples. This collapsing of pores in the sample is gradual and progresses through the sample in form of avalanches. The collapse of the sample is due to mechanical failure and crackling noises often arise in acoustic form because of dynamical features that occur simultaneously with the failure of the sample. The avalanches can then be measured in Acoustic Emission experiments [27].

These acoustic waves result from changes of the internal structure of the material, which leads to a sudden redistribution of internal stress. Acoustic emission occurs, as well, in e.g. dislocation movement and twinning [12].

## 3.1 Crackling noise in porous Vycor

Quite recently acoustic emission experiments to investigate crackling noise were performed in a study of Salje et al., 2011 [27] using Vycor, a porous glass material. They pointed out that the avalanches follow power law statistics with critical exponents similar to those measured in different systems, for example in mechanical instabilities in martensites.

In their measurements, they applied a uniaxial stress and with increasing stress the sample strain changed in steps with simultaneous emission of acoustic waves measured in acoustic emission (AE) experiments. The AE measurements were carried out using different compression rates ( $12.2kPa/s$ ,  $6.5kPa/s$ ,  $1.6kPa/s$ ,  $0.2kPa/s$ ) on four Vycor sample with a pore size of  $7.5nm$ . The samples were prepared having a height of 5mm and different areas ranging from approx. 29 to  $13mm^2$  [27].

In figure 3.1 [27] it can be seen that in the beginning of the experiment low acoustic emission activities could be observed, but high intensities occurred both before and after the sample collapsed due to the applied stress. The size of the collapse and the intensity of crackling noise do not seem to be correlated with each other. The complete collapse of the sample occurred at approx. 15.000s [27].

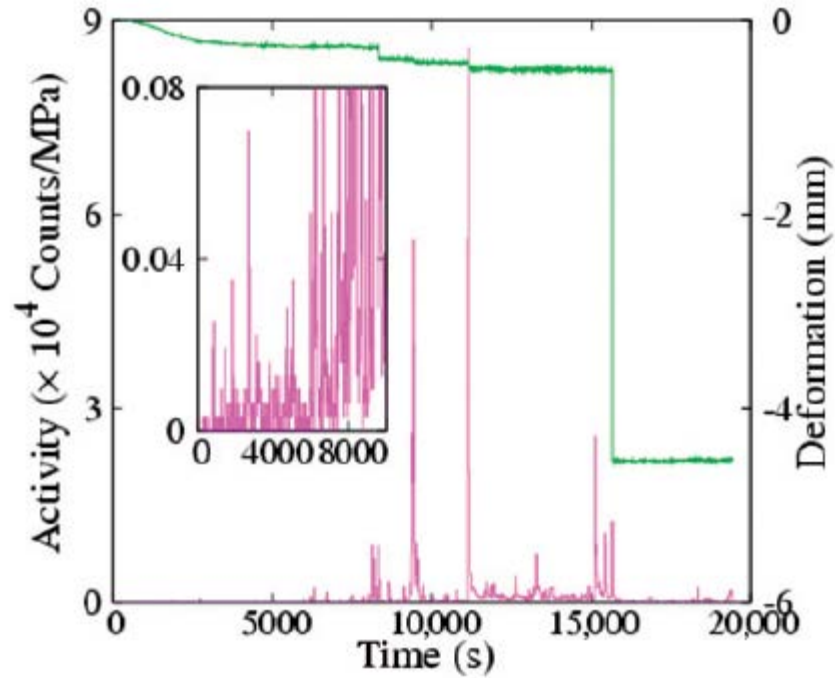


Figure 3.1: AE activity and deformation (at a stress of 1.6kPa/s) of the sample as function of time, inset: low AE activity in the initial part of the experiment [27]

Figure 3.2 depicts the log-log-plot of the energy distribution  $N(E)$  of the AE events and shows that these distributions correspond to power-laws  $N(E) \sim E^{-\epsilon}$  with exponents  $\epsilon$  of approx.  $-1.39$ . This power-law is fulfilled for experiments with a high number of recorded signals over more than six decades of energies. Therefore, evidence is given that the failure mechanisms under compression show avalanche criticality [27].

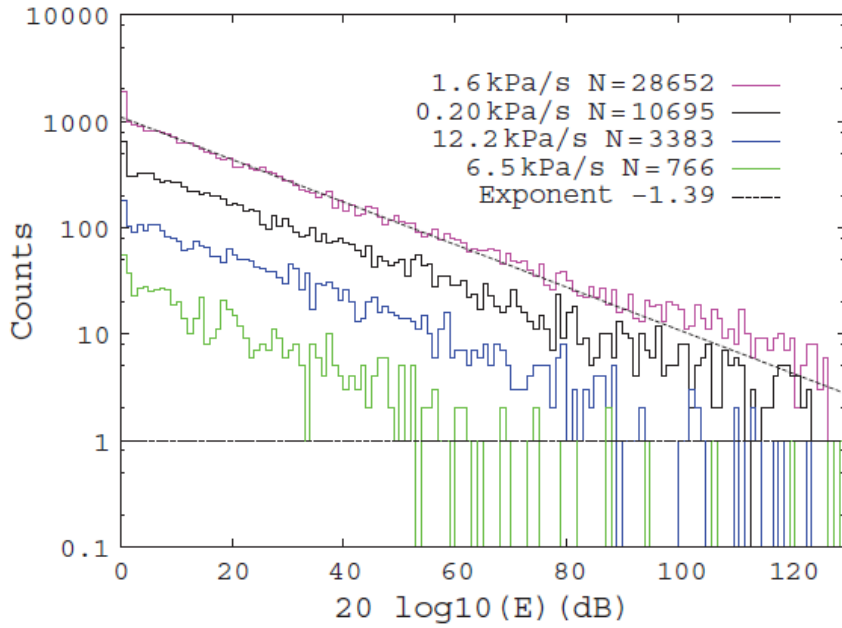


Figure 3.2: Energy distribution of the acoustic emission signals plotted in a log-log-plot. The four curves correspond to four different measurements using different compression rates. The power law exponent of  $-1.39$  is represented by the dashed line [27].

## 3.2 Statistical similarities between compression of porous Vycor and earthquakes

Baró et al., 2013 [4] investigated the statistical similarity between the compression of a porous material, namely Vycor, and earthquakes. They performed uniaxial compression experiments (with three different compression rates:  $0.2\text{kPa/s}$ ,  $1.6\text{kPa/s}$ ,  $12.2\text{kPa/s}$ ) including the simultaneous recording of acoustic emission on this material and examined the failure under compression. Proof was found that the four main laws of statistical seismicity (Gutenberg-Richter law, modified Omori's law, productivity law and unified waiting-time scaling law) are fulfilled yielding stable critical exponents across different experiments [4].

Figure 3.3 shows the AE signal and the sample height as functions of time for one of the compression experiments. Several jumps in the sample height are visible, which cause acoustic emission signals measured as energy avalanches [4].

### 3.2 Statistical similarities between compression of porous Vycor and earthquakes

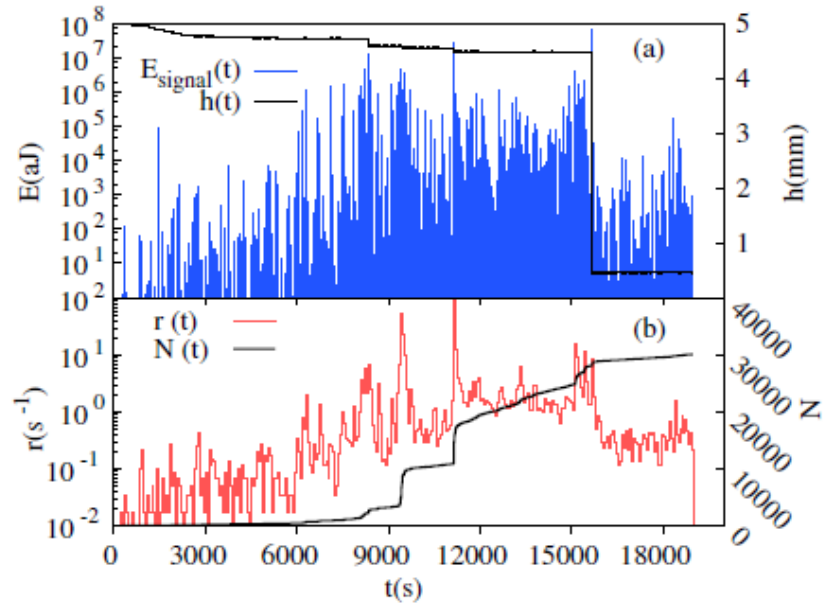


Figure 3.3: AE avalanche energy and change in sample height for a compression experiment with compression rate of  $1.6\text{ kPa/s}$  as functions of time [4].

The avalanche energy distribution, depicted in figure 3.4, follows a power-law  $p(E) \propto E^{-\epsilon}$  with an exponent of approximately 1.39 that is constant for the whole measurement [4].

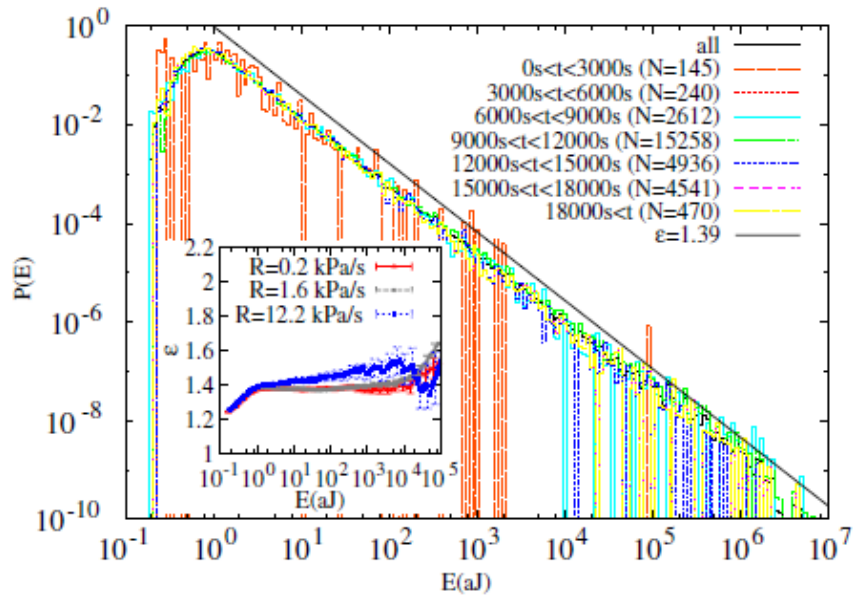


Figure 3.4: Avalanche energy distribution of the experiment with a compression rate of  $1.6\text{ kPa/s}$  and during 7 different subperiods. The straight line represents a power-law with exponent of 1.39 [4].

### 3 Preceding work on crackling in porous materials

Baró et al. also studied the aftershock sequence of the AE signals to compare it to Omori's law. In doing so firstly an energy range of the measured mainshocks has to be determined in order to distinguish between mainshocks and aftershocks. Secondly, after each mainshock the aftershock sequence is analyzed until a new mainshock appears. Figure 3.5 shows the number of aftershocks per unit of time as function of the time difference to the mainshock. Each panel of the figure corresponds to another compression rate. Each curve in figure 3.5 shows approximately the same behavior as the plotted Omori's law with an exponent of  $-0.75$ . Some curves even follow this power-law for up to 6 decades [4].

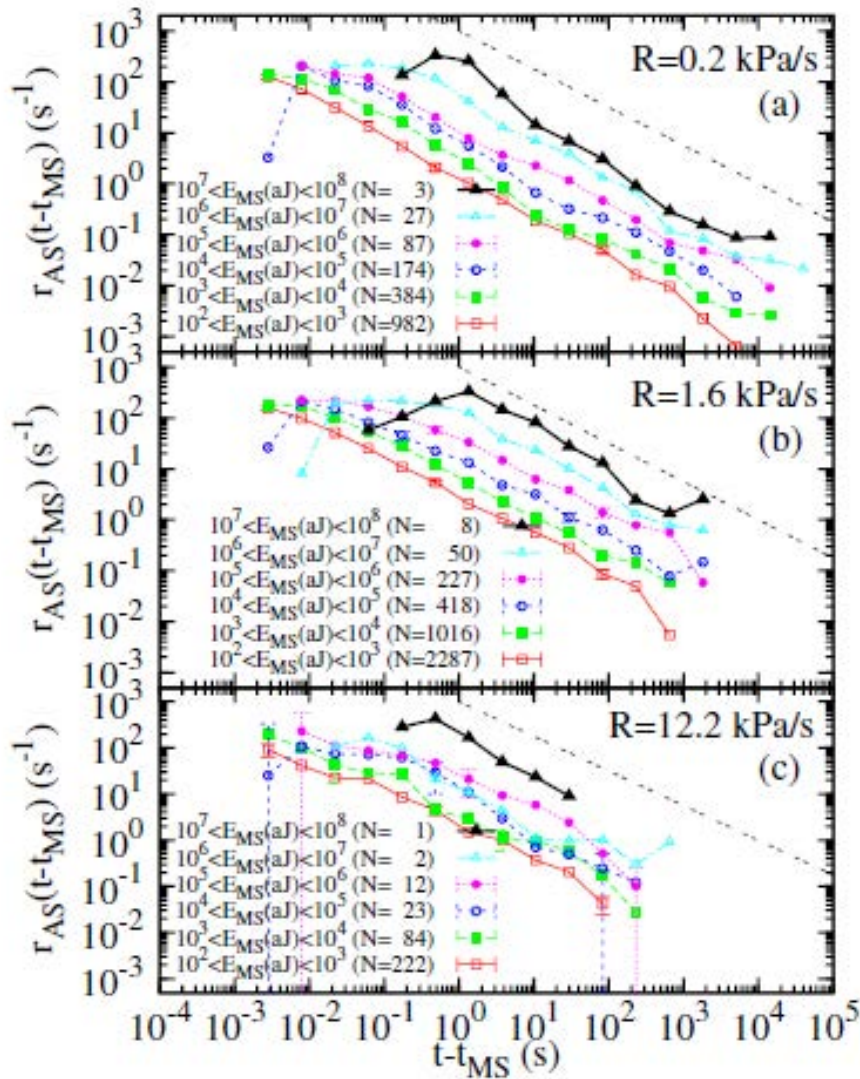


Figure 3.5: Number of aftershocks per unit of time as function of time difference to the mainshock. The dashed line represents Omori's law with exponent of  $-0.75$ . The legend in each panel shows how the mainshocks are defined [4].

### 3.3 Crackling noise in synthetic and natural SiO<sub>2</sub>-based materials

Nataf et al. [23] studied the acoustic emission activity and the jerky changes in sample height of porous SiO<sub>2</sub> based materials in uniaxial compression experiments using compression rates ranging from  $0.2kPa/s$  to  $2.8kPa/s$ . They measured different mesoporous silica ceramics including Gelsil with pore diameters of 2.6 nm and 5 nm, which is a porous synthetic SiO<sub>2</sub> glass material, similar to Vycor, and sandstone, which is a natural porous sedimentary rock. The sample heights and their changes were measured with a laser extensometer with a nominal resolution of 100 nm [23].

Figure 3.6 shows the experimental results of Gelsil 2.6 including the (a) sample height, (b) square of the time derivative of the sample height and (c) AE activity, each as function of time. Inspecting figure 3.6 it seems obvious that the AE activity corresponds well with the square of the jerk velocity ( $\frac{d^2h}{dt^2}$ ). Therefore, the authors assume that there is a certain relation between the AE signals and the energy dissipation resulting from crackling of the sample including its failure [23].

It is one of the main aims of the present work to test if this correspondence between the AE activity and measured strain drops during mechanical failure really holds true.

### 3 Preceding work on crackling in porous materials

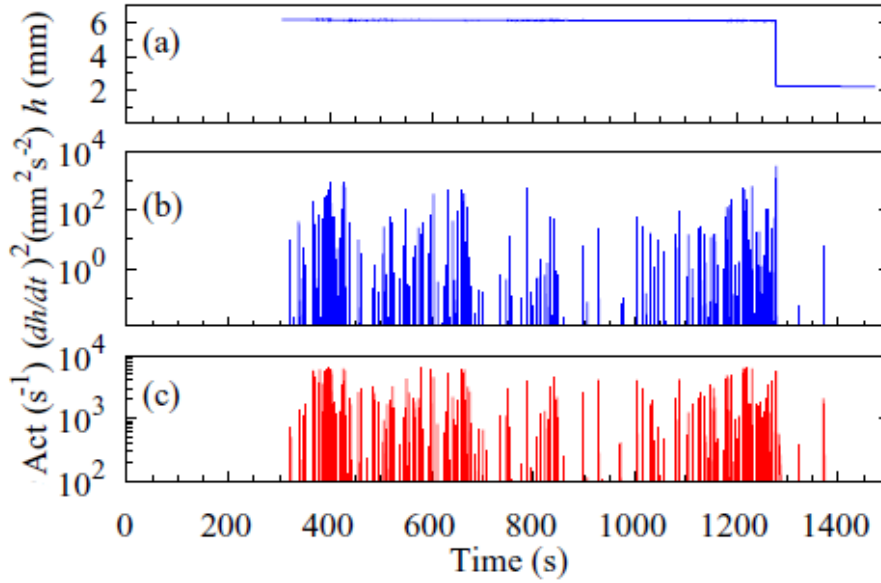


Figure 3.6: Gelsil 2.6 - (a) Sample height, (b) square of its time derivative, (c) AE activity [23]

A comparison between AE signals and changes in sample height was also made for other samples as Gelsil 5 and sandstones, and yielded similar results. Moreover, Nataf et al. analyzed the energy distribution, the number of aftershocks and the distribution of waiting times. The energy distribution for the data obtained for Gelsil 2.6 follows a power-law behavior over several decades and can be fitted with a power-law exponent of about 1.37. For sandstone similar data were obtained and an exponent of about 1.48 was estimated. The distribution of aftershocks plotted in Omori diagrams yielded Omori exponents of about 0.71 and 0.78 for Gelsil and sandstone, respectively [23].

Figure 3.7 shows the energy distributions of the AE events for all samples, including previously measured Vycor, as power laws. The dashed line here corresponds to an exponent of 1.45 [23].

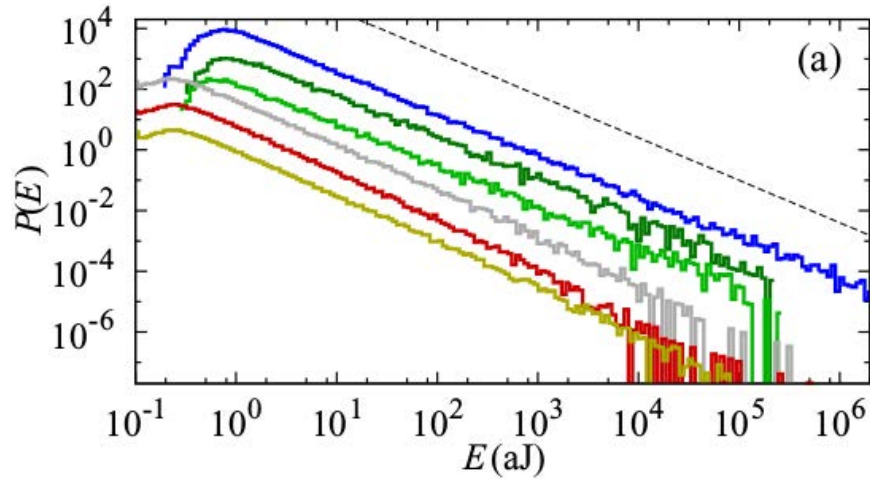


Figure 3.7: Log-log plot of energy distribution of AE events: from top to bottom curves correspond to Vycor, Gelsil 5nm, Gelsil 2.6nm, Light-gray sandstone, red sandstone and yellow sandstone, respectively. All curves, except for Vycor, are shifted for clarity [23]

Tabular 3.1 shows the Omori's exponent  $p$  and exponent of the energy distribution  $\epsilon$  fitted individually for the different samples of Gelsil 5nm and Gelsil 2.6nm which they studied during their work [23]. For completion, the exponent values of Vycor measured by Baró et al. [4] are also added in this tabular.

Table 3.1: Critical Exponents fitted for the different Gelsil samples [23] and for Vycor [4]

<b>Samples</b>	$\epsilon$	$p$
Gelsil 2.6 (1)	$1.37 \pm 0.03$	$0.71 \pm 0.04$
Gelsil 5nm (1)	$1.35 \pm 0.03$	$0.70 \pm 0.04$
Gelsil 5nm (2)	$1.37 \pm 0.03$	$0.77 \pm 0.04$
Vycor	$1.40 \pm 0.05$	$0.75 \pm 0.1$



## 4 Laboratory equipment

This chapter attempts to give an overview as well as a brief description of the used tools and softwares for the performed measurements. For sample preparation the *IsoMet<sup>TM</sup> Low Speed Saw* was used and the measurements themselves were then carried out using the *Perkin Elmer Diamond DMA* and the *Perkin Elmer DMA series 7e*. The DMA measurements were controlled and configured via the software *Pyris Muse System Software*. For evaluation and analysis of the data *OriginPro 2015G* was used.

### 4.1 Measurement tools

#### 4.1.1 IsoMet<sup>TM</sup> Low Speed Saw

For cutting and preparation of the samples a precision sectioning saw from the company *Buehler* was used. The tool itself is called *IsoMet<sup>TM</sup> Low Speed Saw* [20].

As the samples favored for measurements are brittle materials, it is important to pay specific attention to their cutting. The edges of each sample should be as parallel as possible in order to ensure an even compression during the measurements. As well, the deformation of the material possibly occurring during the preparation should be kept to a minimum. Therefore, a precision saw is beneficial for cutting the materials. The cutting with this tool is rather slow using speeds up to *300rpm* and the blade is a diamond wafering blade. Therefore, the damage and deformation of the sample is rather low and the cut surface is of good quality [21], [20].

#### 4.1.2 Dynamic Mechanical Analyzer

A DMA is usually used to analyze the dynamic viscoelasticity (or viscosity) of a material (usually a polymeric material or similar) [13]. This is done via a compression of the sample

#### 4 Laboratory equipment

under stress oscillating with time. As a result of the applied sinusoidal stress the sample gets compressed and recovers again. This can be measured just as well as other responses of the sample apart from its behavior under stress (constituting stress-strain experiments) like its response to different frequencies or temperatures [22], [13].

It is also possible to measure the creep recovery and stress relaxation [13] and derive information about different moduli (like the complex and elastic moduli) [22] of the samples.

When using the DMA the force can be applied in different ways, for example, either in a twisting motion producing a torsion of the sample or axially along one axis of the sample [22]. In case of an applied uniaxial stress in z direction, a relationship between the applied stress  $\sigma$  and the resulting strain (or deformation) of the sample  $\epsilon$  is obtained in the form of [16]:

$$E = \frac{\sigma}{\epsilon} \quad (4.1)$$

E being the Young's modulus.

The applied force is generated as AC and DC force by a function generator [13] and is then transferred to the sample via a rod of metal or quartz [16]. The differential transformer (a so called LVDT) is then responsible for detecting the deformation of the sample [13]. The LVDT (linear variable differential transformer) is able to measure the distance variation of the rod by coils and, thus, the deformation of the sample and the Young's modulus can then be calculated [16]. The accuracy of the distance measurement using the *Perkin Elmer Diamond DMA* is approx.  $10nm$ . The temporal resolution is about  $1s$ .

Regarding the sample fixture geometries of the DMA, different methods are available, for example, fixtures for a three-point or four-point bedding, or cantilever fixtures or parallel plate fixtures [22]. (For detailed information, see *Menhard, 1999, p84.*)

Another property that can be analyzed using a DMA is a material's behavior to changing temperatures, leading to different moduli of the sample [22]. In the case of the used *Pyris Diamond DMA* of the company *PerkinElmer* a temperature range of  $-150^{\circ}C$  to  $600^{\circ}C$  [13]

is adjustable.

Given that for crackling noise analysis jumps in the strain during a compression of the material are of main interest, the DMA is used in TMA mode and an increasing compressive force is applied.

TMA refers to *thermomechanical analysis* and while using TMA mode the sample is compressed via a static force and the deformation and dimensional changes of the sample are being examined. Usually TMA refers to a measurement technique in which the thermal expansion of the sample is measured [22].

Regarding the sample geometry for the experiments performed during this work, only a parallel plate fixture was used and the force was applied axially along one axis of the sample. Besides, the force was applied at constant rate, differently to usual dynamic viscoelasticity measurements with sinusoidal applied stress [22]. Using this DMA, an application of stress till  $10N$  is possible. A home-made holder was used in some later experiments to increase the maximum force by a few Newtons.

Temperature variations were not of interest, therefore no settings were made in the temperature control mode. Altogether, for performing these experiments the DMA was somehow diverted from its usually intended use for soft polymeric materials to brittle and porous materials and minerals.

In figure 4.1 the fixture of the sample in the DMA can be seen. The lower plate is fixed via four screws and the sample is placed in the center of the plate below the upper smaller plate. The stress is applied via the upper plate.

#### 4 Laboratory equipment

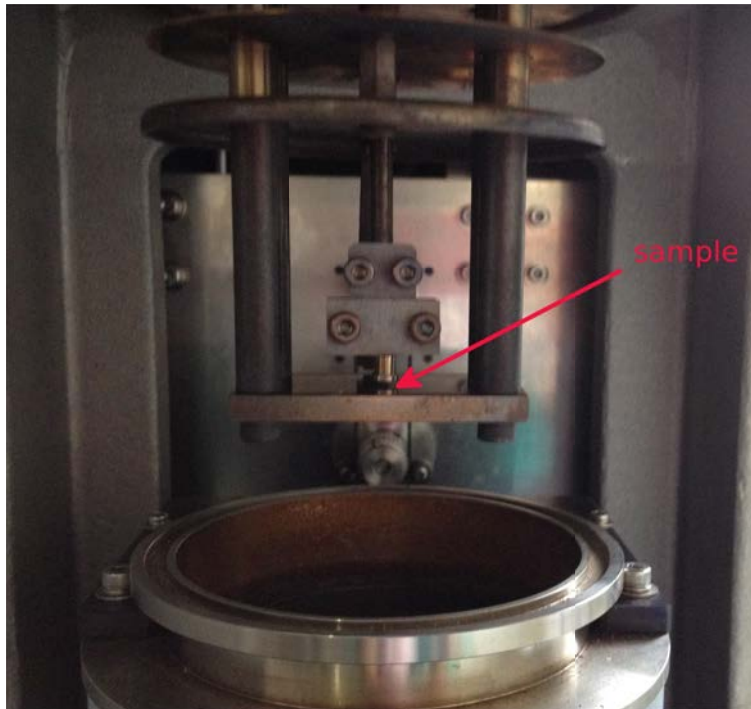


Figure 4.1: Fixture of the sample in a parallel plate setup in the *Perkin Elmer Diamond DMA*

The dimensions of the sample and geometry using the parallel plate fixture is depicted in figure 4.2, which is taken from the measurement condition editor of the measurement software *Pyris Muse System Software*.

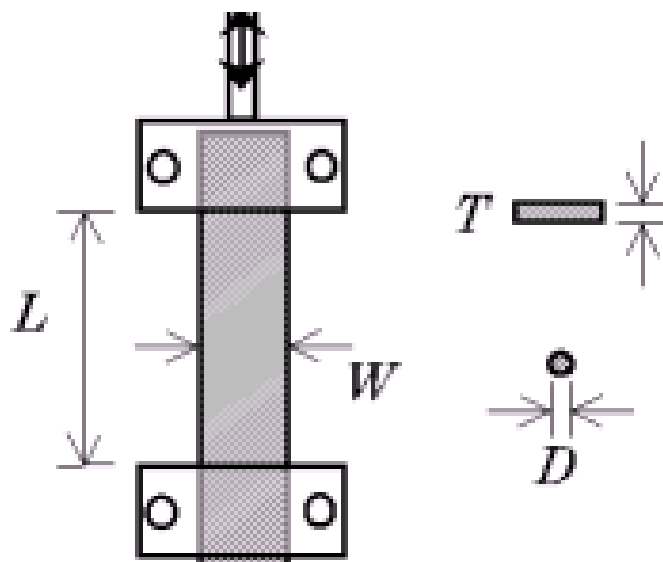


Figure 4.2: Dimensions of the sample in the parallel plate fixture

For the performed measurements both the *Perkin Elmer Diamond DMA* and the *Perkin Elmer DMA series 7e* were used. Although the Diamond DMA is a newer device, its resolution is not as good as the resolution of the Elmer DMA 7e which features a one order of magnitude better time resolution and distance resolution.

As the DMA 7e has such a superior resolution it is also quite sensible to vibrations and is therefore placed on a heavy granite plate positioned on top of a rubber-like material. The measurements are carried out using a parallel plate measuring system as well. Using the DMA 7e a force up to  $8N$  can be applied to the sample.

## 4.2 Measurement & data evaluation software

The software used for measuring with the *Perkin Elmer Diamond DMA* was the *Pyris Muse System Software* version 3.9U (Build 716) from *SII NanoTechnology Inc., 2001-2004*. The software used with the *Perkin Elmer DMA series 7e* was the *Pyris Software* version 8.0.0.0172 from *Perkin Elmer, 2006*. These Softwares are thermal analysis softwares and while using them, different measurement methods and modes (e.g. TMA mode for stress-strain measurements) and conditions can be used. Additionally, customized temperature programs can be selected.

For data evaluation the software *OriginPro 2015G* of *OriginLab Corp.* was used.



# 5 Samples and sample preparation

This chapter focuses on the different samples used for the measurements and their preparation. For this study, brittle, porous materials were of great interest, as introduced in chapter 3. Therefore, Shale, Vycor and Gelsil were selected.

## 5.1 Samples

### 5.1.1 Shale

Shale stone is a sedimentary stone and belongs to the group of fine-grained clastic sediments, which includes for example clays and mudstones as well. These rocks are also referred to as mudrocks or argillaceous rocks, because they consist of little, differently sized fragments of clay and silt. A main distinction is made between minerals able to split along parallel planes of lamination and those not possessing this property called 'fissility'. Shales belong to the group of fissile minerals, whereas mudstones show non-fissile properties [10], [14].

The samples used for the measurements were prepared using Shale stones as can be seen in figure 5.1. Next to the big raw Shale stones, one tiny Shale sample that has already been prepared is (barely) visible on the image. (Its size is about  $1\text{mm} \times 1\text{mm} \times 1\text{mm}$ .)



Figure 5.1: Shale stones used for sample preparation

### 5.1.2 Vycor

Vycor is the trademark of a porous glass material which was found and produced seeking for glasses with properties superior to those of ordinary glasses, especially concerning heat shock resistance and resistance to deformation. For preparation of these glasses a rather soft alkali-borosilicate glass is melted and then molded to the desired shape according to standard glass processes. Afterwards it is subject to a heat treatment above the annealing point, which leads to a phase separation. The phases formed are two glassy phases, one (acid-soluble) phase rich in alkali and boric oxide, the other (insoluble) phase being rich in silica. After the heat treatment the acid-soluble phase is dissolved (leaching) and the silica-rich and porous phase remains and is further consolidated via heating it to  $> 1200^{\circ}\text{C}$ . The pore size distribution of commercial porous Vycor glass is usually quite narrow and the average pore diameters are about  $8 - 12\text{nm}$ . (96% of the pores are  $\pm 0.3\text{nm}$  from the average pore radius.) The Company Corning Inc. produces and distributes these porous glasses under the trademark Vycor 96%  $\text{SiO}_2$  glass. [7]

Vycor used for measurements had an average pore diameter of  $7.5\text{nm}$ .

### 5.1.3 Gelsil

Gelsil, like Vycor, is a SiO<sub>2</sub>-based synthetic material, but has a different porous mesostructure. Gelsil is produced by a company named *4F International Co.* from Gainesville, FL in a sol-gel process by hydrolization of silica containing precursor liquids which is then followed by condensation and heat treatment. Within the hydrolized silica precursor, the silica molecules condensate to spheres on stochastic sites. A network-like arrangement of spheres is then obtained after gelation. In the end a material is obtained which can be imagined as an assembly of stochastically arranged and monodisperse pure silica spheres. The voids between these spheres exhibit a larger pore size distribution than Vycor 7390 and the mean void diameter is about 2.6 and 5nm for Gelsil 2.6 and Gelsil 5, respectively. [16], [23]

Figure 5.2 shows Gelsil 2.6nm cylinders that were used to prepare small samples. In this image the samples appear yellowish due to contamination with organic molecules [16]. The samples have to be cleaned so that the pores are free of any dirt that could have influence on the crackling behavior.

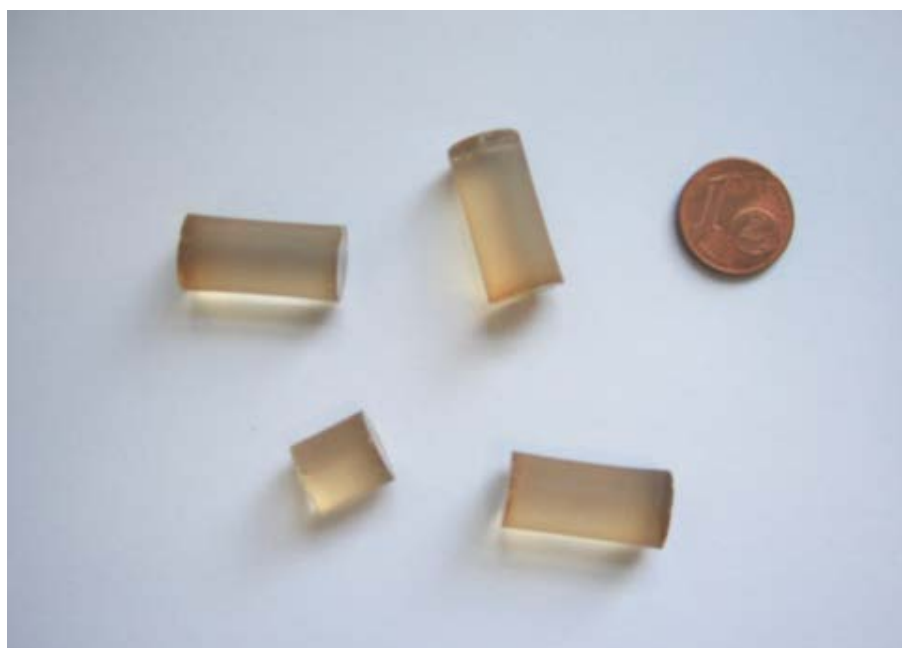


Figure 5.2: Gelsil used for sample preparation [16]

## 5 Samples and sample preparation

Tabular 5.1 shows some characteristics of the studied Gelsil and Vycor samples.

Table 5.1: Characteristics of the studied Gelsil and Vycor samples according to refs [9], [17]

Sample	Vycor 7.5nm	Gelsil 5nm	Gelsil 2.6nm
Average pore diameter (nm)	7.5	5	2.6
Porosity $\Phi$ (%) (1)	40	54	59
Density ( $g/cm^3$ )	1.9	1.2	1.2
Surface area ( $m^2/g$ )	70	510	590
Approx. failure stress $\sigma_f$ (MPa)	50	10	0.5

Regarding their porous structure, Vycor and Gelsil differ slightly: Gelsil is composed of randomly distributed spheres, whereas Vycor consists of interconnected pores and pockets. The difference is depicted schematically in figure 5.3 [16].

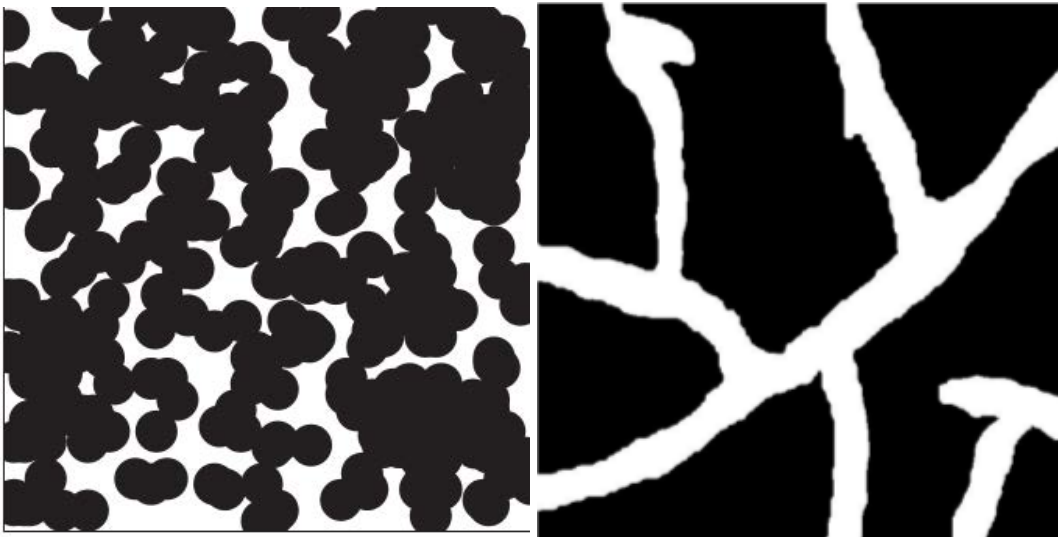


Figure 5.3: Comparison between the porous mesostructures of Gelsil (left) and Vycor (right) [16]

Figure 5.4 shows how a typical compression experiment using this porous samples looks like. The indicated scale labelling 7.5nm corresponds to the pore size of the used Vycor samples [30].

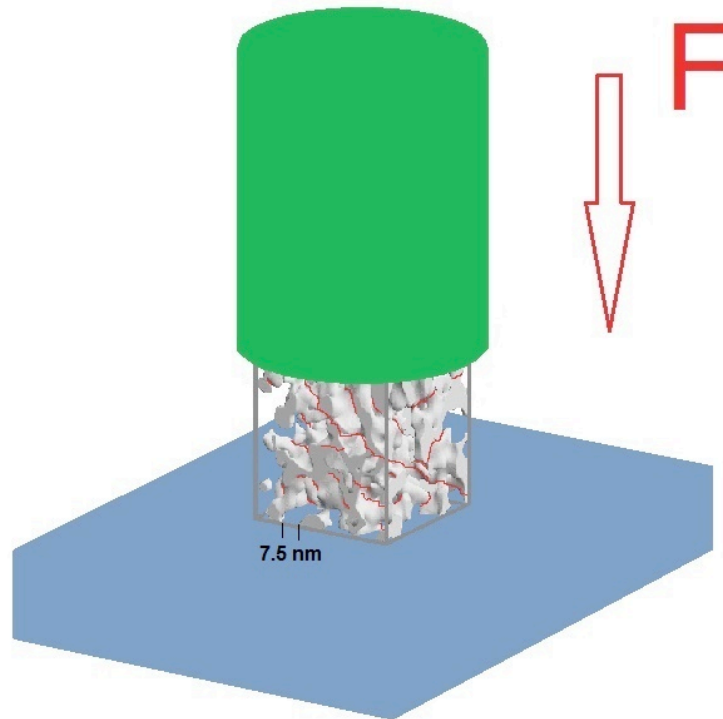


Figure 5.4: Geometry of a typical compression experiment of a porous material using a DMA [30]

## 5.2 Sample preparation

For the cutting of the samples the *IsoMet<sup>TM</sup> Low Speed Saw*, see section 4.1.1, was used. The pieces, which were cut from a larger Shale stone or Vycor/Gelsil piece, were then in turn cut into small parallelepipeds using a precision hand saw with diamond wire and further polished with a polishing paper to obtain even smaller sample sizes with edges free of considerable surface irregularities. Figure 5.5 shows the tools and utilities that were used for preparing the samples, including a precision hand saw, fine tweezers, a digital sliding caliper and a polishing paper. (The bluish foam material was used for cutting the samples with the hand saw.)



Figure 5.5: Tools and utilities used for sample preparation

It is important to ensure that the sample consists of nearly parallel edges, as this lowers the risk of influences on the measurement from a shearing of the sample under stress.

# 6 Measurement procedure

This chapter covers the measurement process using the Diamond DMA (DDMA) and the DMA 7e. All samples of Gelsil, Vycor and Shale are listed including their height and cross section. Compression experiments were performed at constant low compression rates of about  $0.1\text{mN/s}$ – $10\text{mN/s}$  and different types of compression settings were used, including single compression ramp measurements and stress cycling measurements.

## 6.1 Shale

### 6.1.1 Samples and measurement set-ups

For the crackling measurements on Shale, various samples were prepared, each in different sizes. For the preparation of these samples, small pieces of Shale were first cut using the *IsoMet<sup>TM</sup> Low Speed Saw* and afterwards further cut with a precision hand saw and polished with a polishing paper, as explained in section 5.2.

In tab. 6.1<sup>1</sup> a list of all the Shale samples investigated can be seen. All measurements of Shale were performed using the *Perkin Elmer diamond DMA*.

---

<sup>1</sup>The measurement uncertainty results from the (digital) sliding caliper  $\pm 0.01$  which was used for measuring the dimensions of the sample.

## 6 Measurement procedure

Table 6.1: List of Shale samples including their heights and cross sections

No.	Height [mm]	Cross section [mm <sup>2</sup> ]
1	2.20 ± 0.01	1.369 ± 0.03
2	1.40 ± 0.01	1.16 ± 0.03
3	0.97 ± 0.01	1.08 ± 0.03
4	0.94 ± 0.01	1.09 ± 0.03

Tabular 6.2 shows the different measurement settings for the Shale measurements. (For all measurements, the force was applied until it reached the maximum value of 10N. As the stress is applied in downward direction, the force is actually negativ, e.g. from -10mN to -10N.) Columns 'Stress min' and 'Stress max' refer to the stress at the beginning of each compression ramp until the end. For the maximum stress always the maximum possible stress for the DMA was used.

The column 'R' denotes the different compression rates and the column 'mode' refers to the way in which the force was applied during the whole measurement: 'Cycle measurement' states a measurement in which the compression ramp was repeated once the maximum force of 10N was reached resulting in a cycle measurement. 'Single ramp' describes a measurement in which after reaching the maximum force the measurement was stopped and 'Single ramp + constant force at 10N' refers to a measurement in which after reaching 10N the force was hold constant at its maximum value for a defined time interval (in case of Shale for about 5000s), then set to its initial value again, and the measurement was stopped.

Table 6.2: Measurement settings for the Shale samples of tabular 6.1

No.	Stress min [mN]	Stress max [mN]	R [mN/min]	Mode
1	10	10000	10	cycle measurement
2	10	10000	1	single ramp
3	10	10000	2	single ramp + constant force at 10N
4	10	10000	2	single ramp + constant force at 10N

## 6.1.2 Shale measurements

For the first Shale measurement, the first Shale sample (see tabular 6.1) was used. Figure 6.1 shows the sample height, applied force and calculated squared drop velocity values  $v_m^2 = (dh/dt)_m^2$  which are assumed to be proportional to the released energy during the breaking of pores and, comparable to the energies measured in acoustic emission experiments.

The energies involved in one strain burst can be estimated by  $E_m = \frac{Mv_m^2}{2}$ . The moved mass  $M$  is assumed to be of the order of the sample mass of about  $M \propto 10^{-7}kg$ . As  $v_m$  values are measured in the range of  $1nm/s - 1000nm/s$  the estimated burst energies are in the range of  $10^{-5} - 10^1 aJ$ . Another estimation can be made with the change in elastic energy resulting from a crack of size  $a$ :  $E_{el} \propto \frac{\sigma^2 \cdot a^3}{E}$  with the applied stress  $\sigma$ , the Young's modulus  $E$  and typical crack size  $a$ . Assuming  $\sigma \approx 1MPa$ ,  $E \approx 100GPa$  the elastic energy release during the collapse of one pore of a typical pore size  $a \approx 10nm$  (which is an estimate for Vycor) can be estimated as  $E_{el} \approx 10^{-5} aJ$ . As these two estimations are in good agreement, it is assumed that the elastic energy released by the collapse of pores can be well determined by measuring the squared drop velocities [30].

It is visible in figure 6.1 that during the first Shale measurement the applied force was not strong enough to break the sample. The green curve in figure 6.1 represents how the sample height changes with applied stress. As the stress is set to its initial value, the sample relaxes and with increasing stress, the sample gets compressed again.

For the squared drop velocities of figure 6.1 only negative velocity values were used, whereas the positive values were removed from the data set as they are due to backjumps and elastic recoveries of the sample. For the same reason, the largest peaks at the end of each stress cycle were cut as well before conducting further calculations.

## 6 Measurement procedure

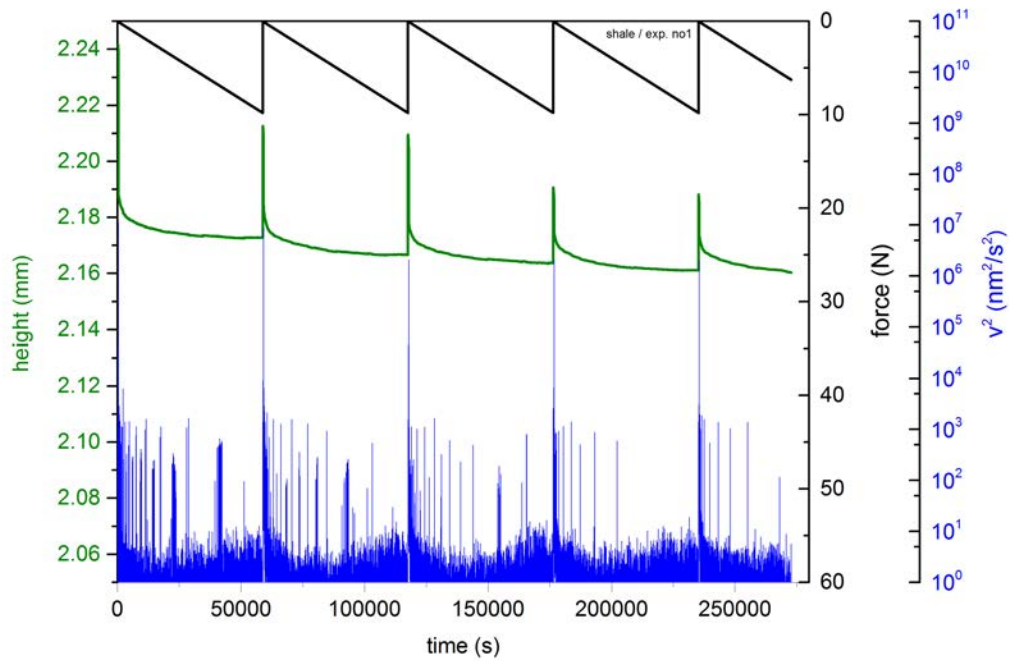


Figure 6.1: Shale 1: Sample height (green), applied force (black) and squared drop velocities (blue) as functions of time (measured with Diamond DMA)

As expected, the sample does not get compressed uniformly and smoothly with increasing stress, but in little jumps and avalanches. In figure 6.2 only the first cycle of the measurement is depicted (til 5500s or approx. 1.5h of the whole experiment, 6.1). In the small cutout, the jerk-like behavior of the compression of the Shale sample can be seen clearly.

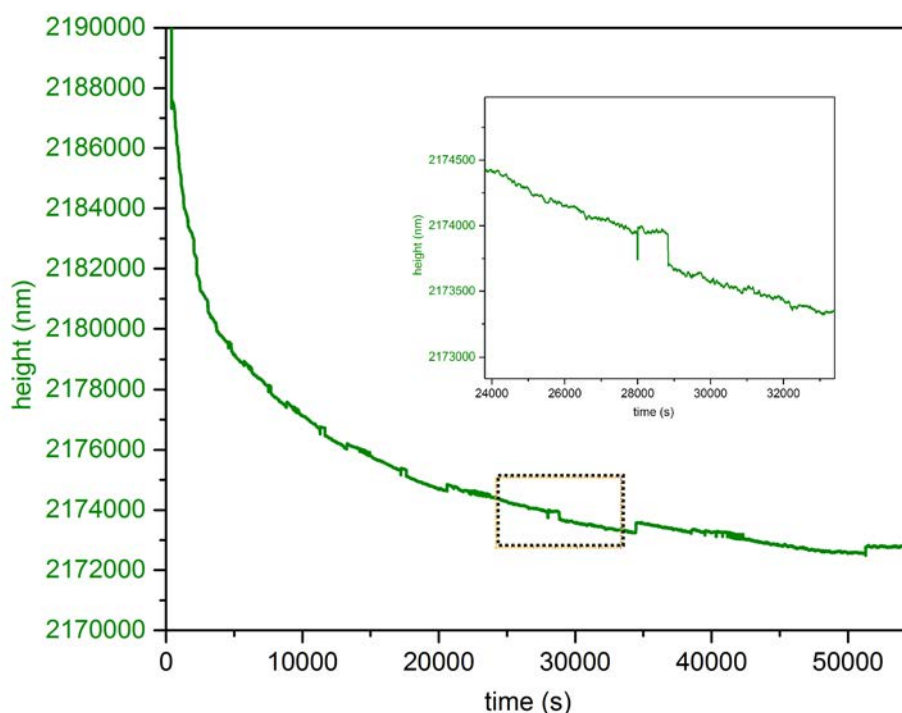


Figure 6.2: Sample height as function of time for the first cycle from measurement time of 0 to 58000s, inset: magnification of a selected area of the plotted curve (measured with Diamond DMA)

The second Shale measurement investigates the second Shale sample according to tabular 6.1. Here, an attempt was made to prepare an even smaller sample than what was used for the previous measurement. Hence, the probability of achieving a complete macroscopic failure of the sample during the compression was increased. (It is assumed that the exponent values deviate slightly in case the sample does not fail at the end of the compression cycles.)

In figure 6.3 the sample height, applied force and the square of the drop velocities are depicted as functions of the time. It is notable that the velocity squared values are increasing with time, which is probably a sign of approaching the failure point of the sample.

## 6 Measurement procedure

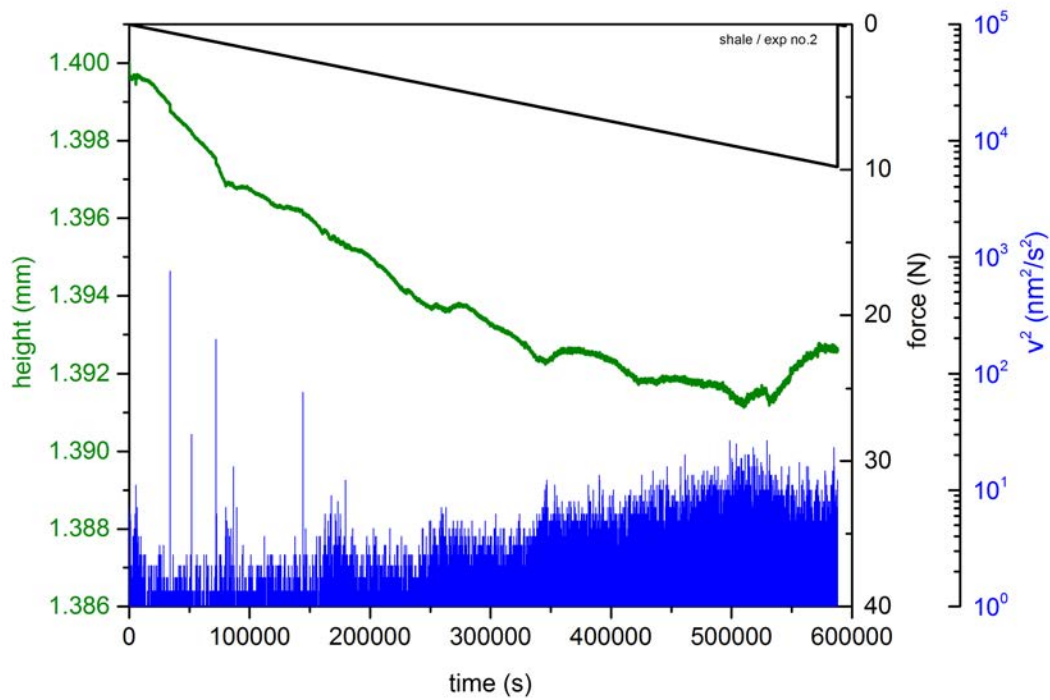


Figure 6.3: Shale 2: Sample height (green), applied force (black) and squared drop velocities (blue) as functions of time (measured with Diamond DMA)

For the third measurement, once again, a new sample was prepared having the dimensions according to tabular 6.1. Figure 6.4 shows the sample height, applied force and the squared drop velocities as functions of the time. During this measurement, some larger backjumps occurred in the sample while the stress was increased.

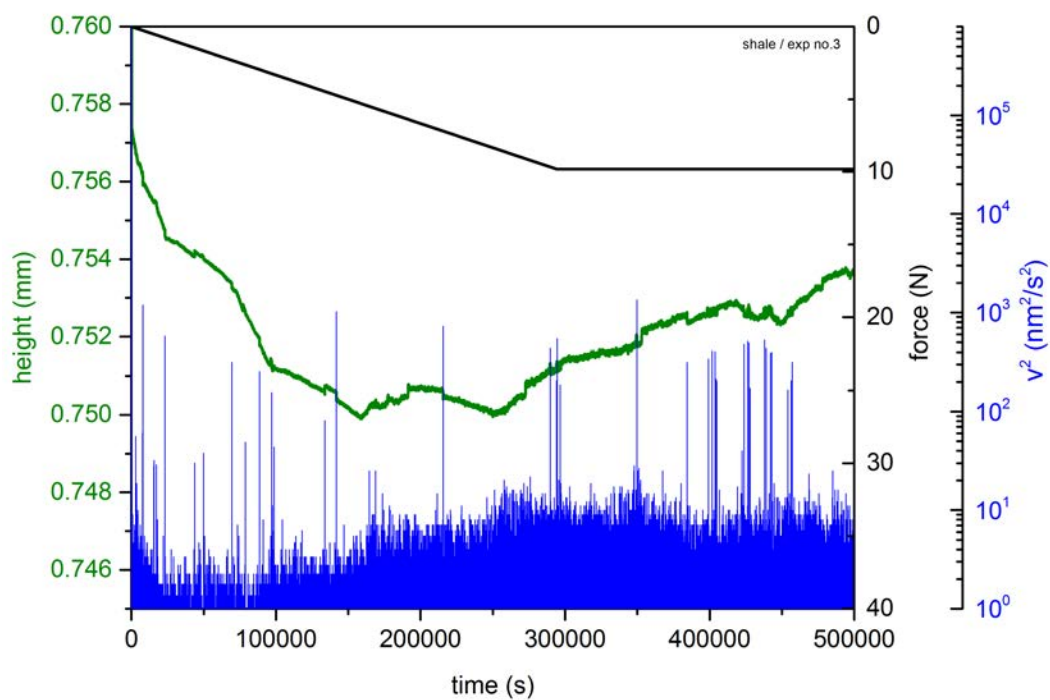


Figure 6.4: Shale 3: Sample height (green), applied force (black) and squared drop velocities (blue) as functions of time (measured with Diamond DMA)

The fourth measurement concerns the sample Shale number 4 (6.1), which is described in figure 6.5 in further detail, noting sample height, applied force and squared drop velocities as functions of time.

## 6 Measurement procedure

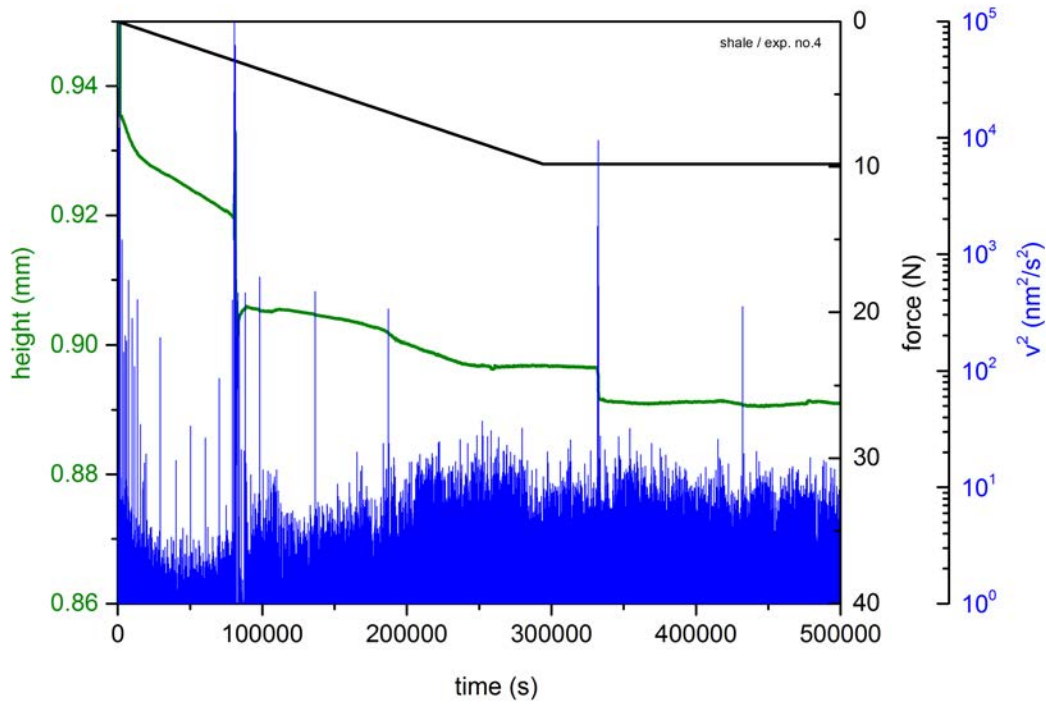


Figure 6.5: Shale 4: Sample height (green), applied force (black) and squared drop velocities (blue) as functions of time (measured with Diamond DMA)

## 6.2 Vycor

### 6.2.1 Samples and measurement set-up

Apart from previous Vycor measurements analyzed, only one sample was prepared according to tabular 6.3 and measured as described in tabular 6.4.

Table 6.3: Vycor sample including its height and cross section

Number	Height [mm]	Cross section [ $mm^2$ ]
1	$1.53 \pm 0.01$	$1.21 \pm 0.02$

Table 6.4: Measurement settings for the Vycor sample of tabular 6.3

No.	Stress min [mN]	Stress max [mN]	R [mN/min]	Mode
1	10	10000	2	single ramp + constant force at 10N

## 6.2.2 Vycor measurements

The first measurement including a Vycor sample applies the same conditions as were used for the 3rd and 4th Shale measurements, described above. The evolution of sample height, applied stress and squared drop velocities are depicted in figure 6.6.

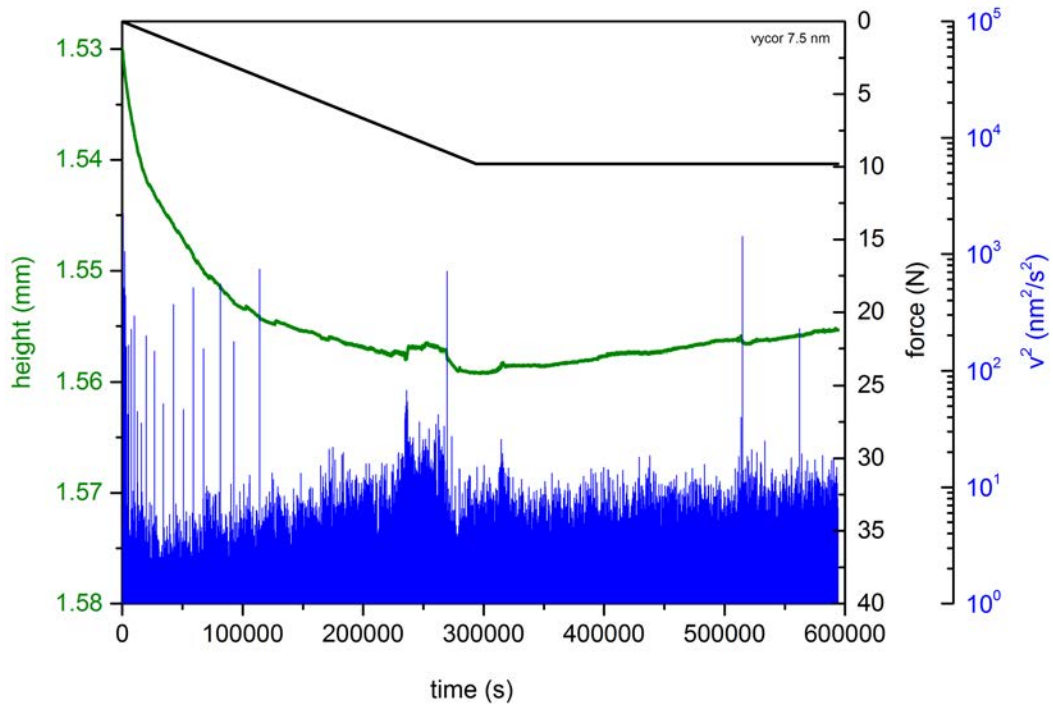


Figure 6.6: Vycor 7.5nm: Sample height (green), applied force (black) and squared drop velocity (blue) as functions of time (measured with Diamond DMA)

Figure 6.7 shows a previous cycle measurement of Vycor that has been performed before the measurements for this work were done [30]. The data of this stress cycling experiment was analyzed and this measurement was found to yield one of the best results with a well defined power-law stable over some orders of magnitude.

## 6 Measurement procedure

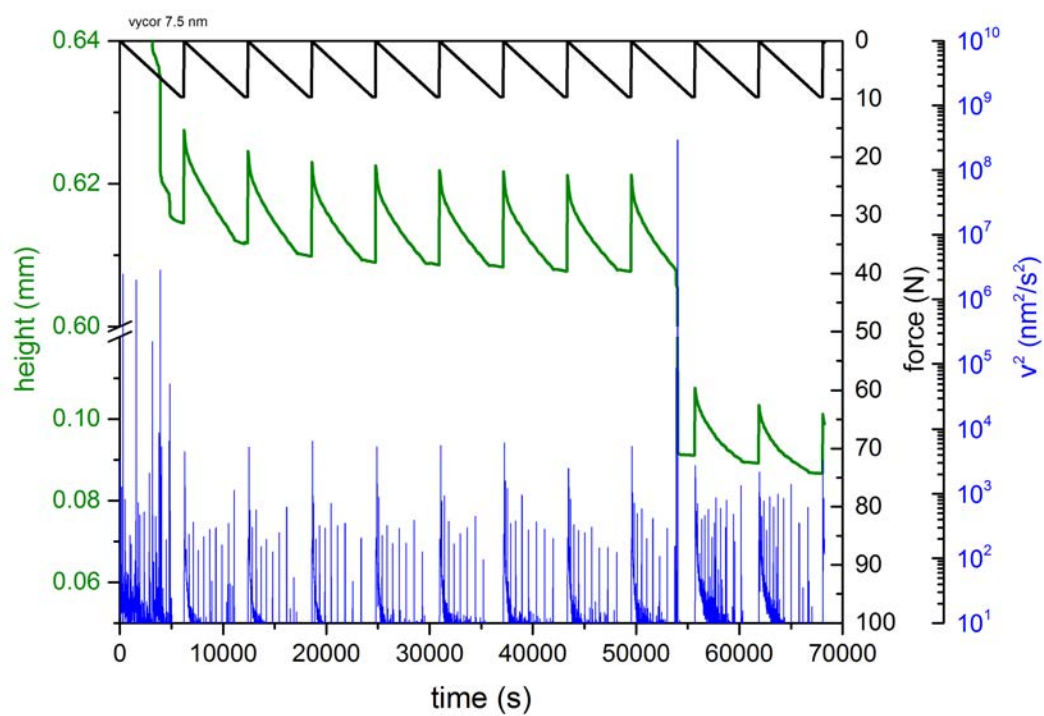


Figure 6.7: Vycor 7.5nm: Sample height (green), applied force (black) and squared drop velocity (blue) as functions of time (measured with Diamond DMA), (With a y-axis break from 0.12mm-0.6mm the evolution of the sample is better displayed.)

## 6.3 Gelsil

### 6.3.1 Samples and measurement set-up

Gelsil 2.6 nm and Gelsil 5nm samples of sizes according to table 6.5 were used for measurements.

Table 6.5: List of Gelsil samples including their void size, height and cross section

No.	Void size	Height [mm]	Cross section [mm <sup>2</sup> ]
1	5nm	1.14 ± 0.01	3.73 ± 0.04
2	5nm	0.71 ± 0.01	1.13 ± 0.02
3	2.6nm	2.19 ± 0.01	1.93 ± 0.02
4	2.6nm	1.58 ± 0.01	5.06 ± 0.05
5	2.6nm	1.48 ± 0.01	5.64 ± 0.06
6	2.6nm	5.17 ± 0.01	5.21 ± 0.06
7	2.6nm	5.02 ± 0.01	5.16 ± 0.06
8	2.6nm	5.02 ± 0.01	4.66 ± 0.05
9	2.6nm	5.16 ± 0.01	1.30 ± 0.02
10	2.6nm	5.24 ± 0.01	4.03 ± 0.04
11	2.6nm	5.02 ± 0.01	5.16 ± 0.05
12	2.6nm	1.67 ± 0.01	2.85 ± 0.03
13	2.6nm	1.86 ± 0.01	3.50 ± 0.04
14	5nm	3.04 ± 0.01	2.22 ± 0.03
15	2.6nm	5.24 ± 0.01	4.03 ± 0.04
16	5nm	3.62 ± 0.01	2.02 ± 0.02

The measurement settings for the Gelsil samples of tabular 6.5 are described in tabular 6.6. Measurements carried out until a maximum force of 8N were performed using the DMA 7e. For measurements number 15 and 16 an additional weight was added as explained in chapter 4.1.2.

Table 6.6: Measurement settings for the Gelsil samples of tabular 6.5

No.	Stress min [mN]	Stress max [mN]	R [mN/min]	Mode
1	100	8000	7	single ramp
2	100	8000	60	single ramp
3	100	8000	6	single ramp
4	10	8000	200	single ramp
5	10	8000	200	single ramp
6	10	8000	15	single ramp
7	10	10000	5	single ramp
8	10	10000	50	cycle measurement
9	10	10000	20	cycle measurement
10	10	10000	20	cycle measurement
11	10	10000	5	single ramp
12	10	10000	100	single ramp
13	10	10000	10	single ramp
14	10	10000	40	cycle measurement
15	10	10000	40	cycle measurement
16	10	10000	40	cycle measurement

### 6.3.2 Gelsil measurements

The following images are examples of Gelsil measurements. Experiments number 15 and 16 were chosen because they yielded the best results. Each image shows the squared drop velocities, sample deformation and applied stress, see figure 6.8 and figure 6.9

During the performance of the experiments, it was detected that stress cycles measurements yielded best results. Moreover, in each of those cycle measurements power-laws stable over more than three orders of magnitudes have been found. Measurements performed with single stress ramp did not yield good results in most cases.

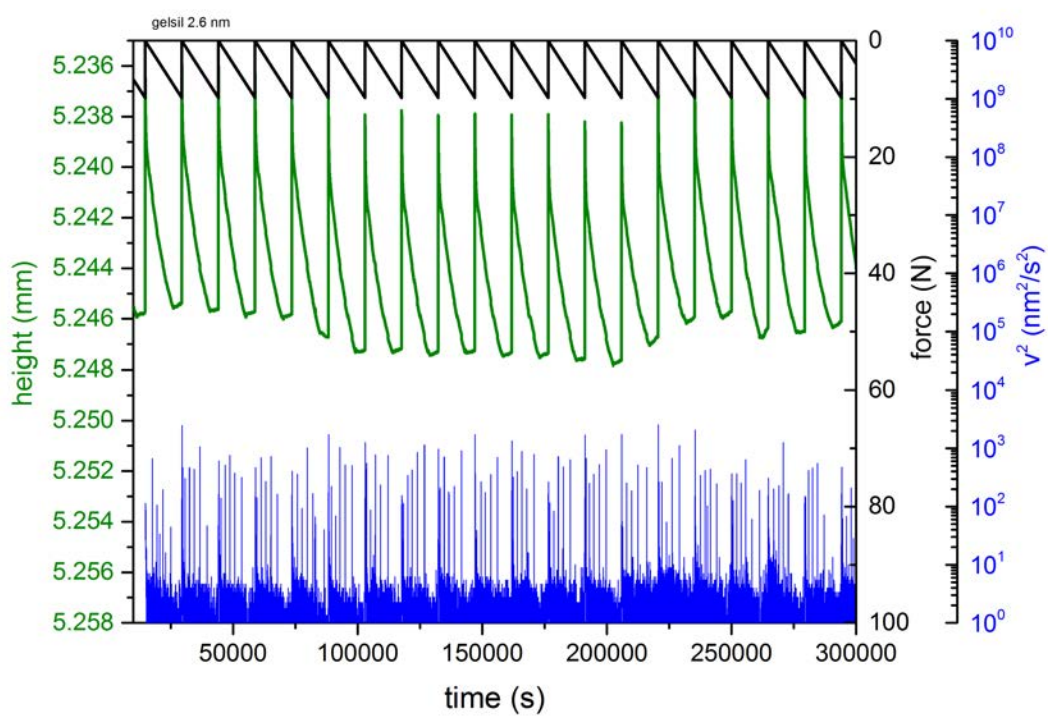


Figure 6.8: Gelsil 2.6: Sample height (green), applied force (black) and squared drop velocity (blue) as functions of time (measured with Diamond DMA)

## 6 Measurement procedure

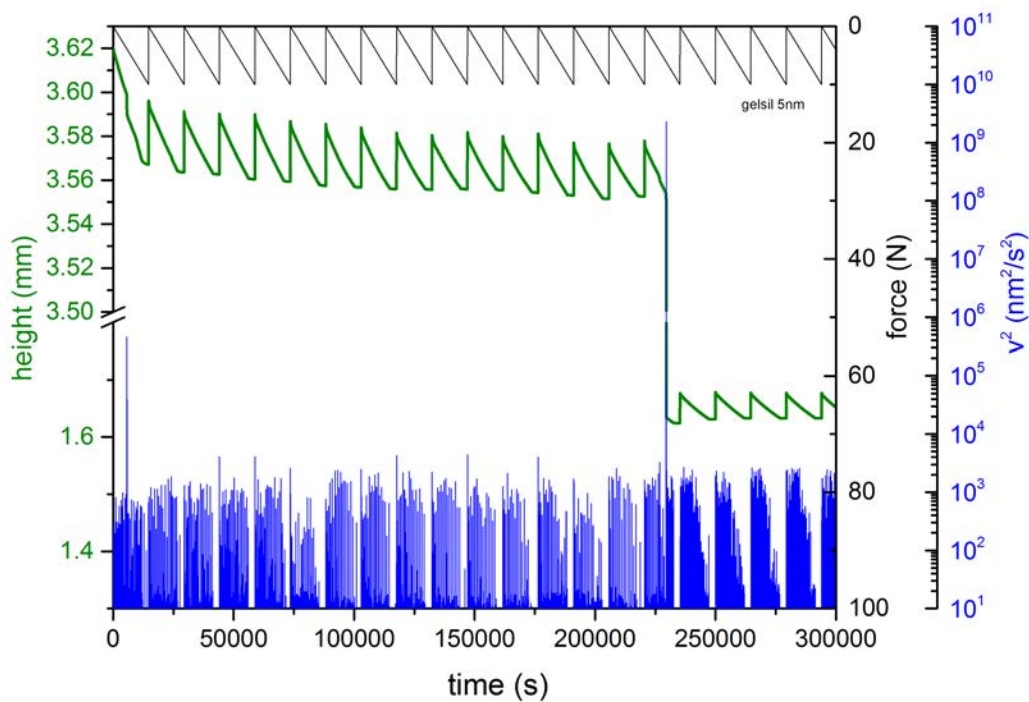


Figure 6.9: Gelsil 5: Sample height (green), applied force (black) and squared drop velocities (blue) as functions of time (measured with Diamond DMA), (With a y-axis break from 1.8mm-3.5mm the evolution of the sample is better displayed.)

Figure 6.10 shows a measurement of Gelsil 5nm with single stress ramp, which has been performed previous to the measurements done for this work [30]. An analysis of these data revealed a roughly defined power-law in the squared drop velocity distribution. Power-laws found in stress cycling are much better defined, which suggests that cycle measurements are indeed superior to single stress ramp measurements.

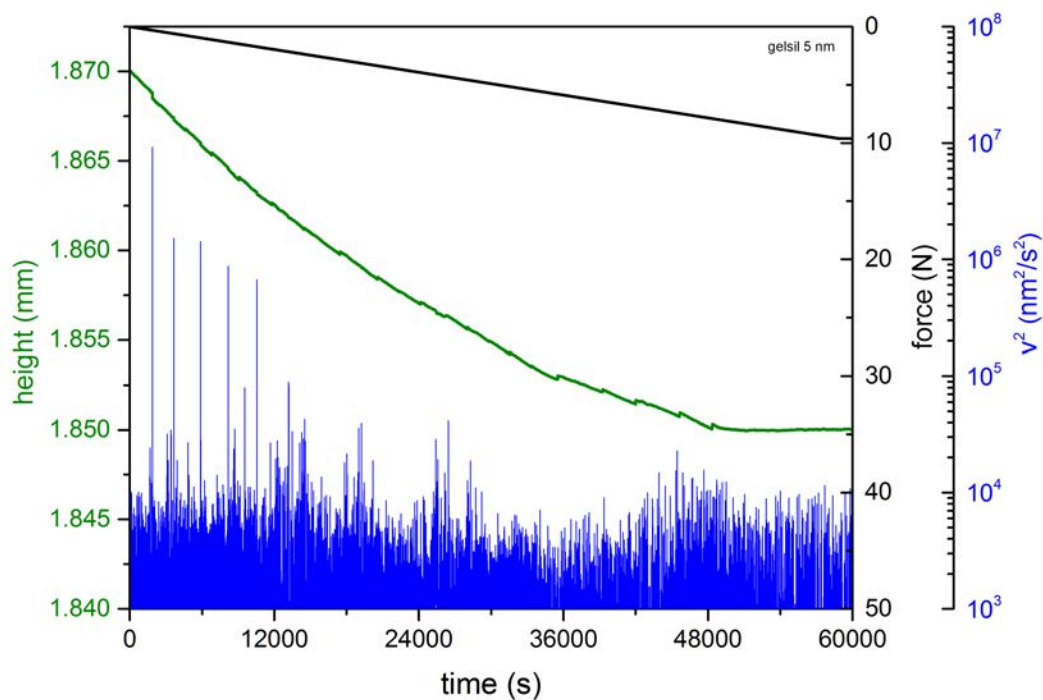


Figure 6.10: Gelsil 5: Sample height (green), applied force (black) and squared drop velocities (blue) as functions of time (measured with Diamond DMA)

Measurements done with the DMA 7e yielded results that were not as good as expected. Although the resolution of this device is superior to that of the Diamond DMA, the data included a considerable amount of noise. It is likely that the crackling events perish in the noise produced by the force motor. The DMA 7e is much more sensible to vibrations than the Diamond DMA and might, therefore, be entirely inefficient when used for such measurements. Figure 6.11 shows an example of the DMA 7e measurement.

## 6 Measurement procedure

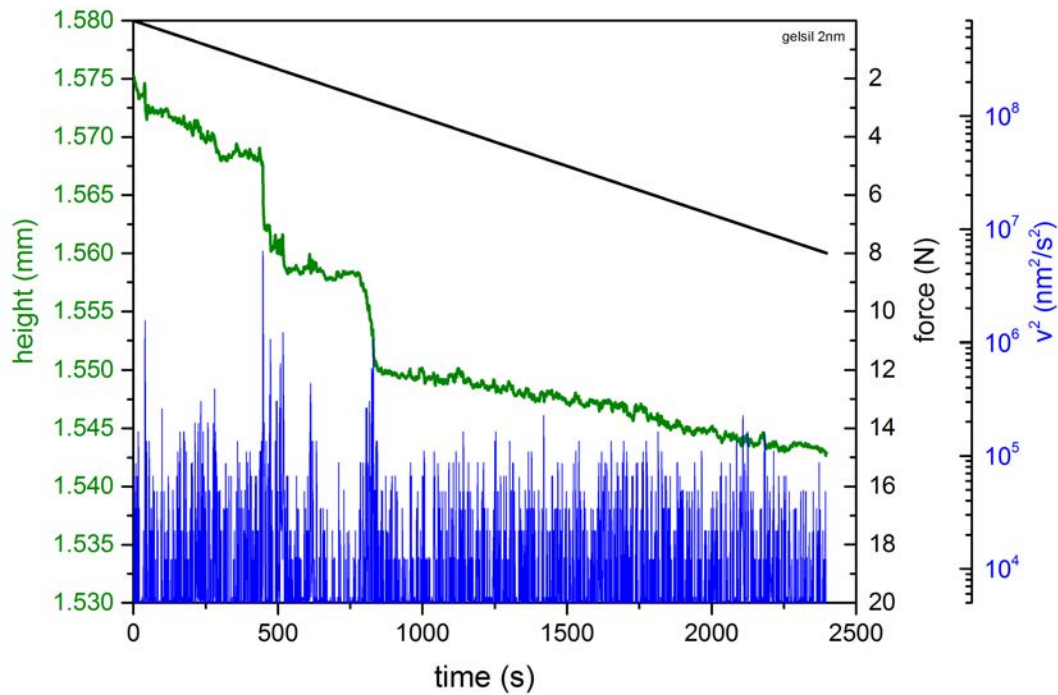


Figure 6.11: Gelsil 2.6: Sample height (green), applied force (black) and squared drop velocities (blue) as functions of time (measured with DMA 7e)

In the following diagrams, namely figure 6.12 and figure 6.13, comparisons of the sample deformation measured by Diamond DMA and DMA 7e are shown. Clearly the DMA 7e measurements cannot be used for determining the crackling behavior of the selected samples, as the measured sample height does not consist of nice defined jerks as in the images from Diamond DMA measurements. The squared drop velocity distribution of the DMA 7e measurements did not show any power-law behavior, as expected due to the noise present in the data.

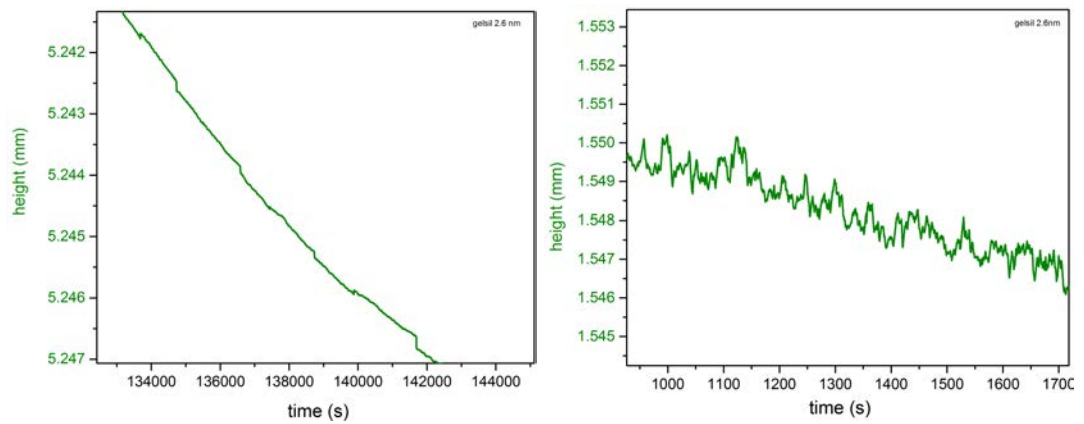


Figure 6.12: Gelsil 2.6: Changes of sample height under compression measured by Diamond DMA,  $R=40\text{mN/s}$  (left) and DMA 7e,  $R=200\text{mN/s}$  (right)

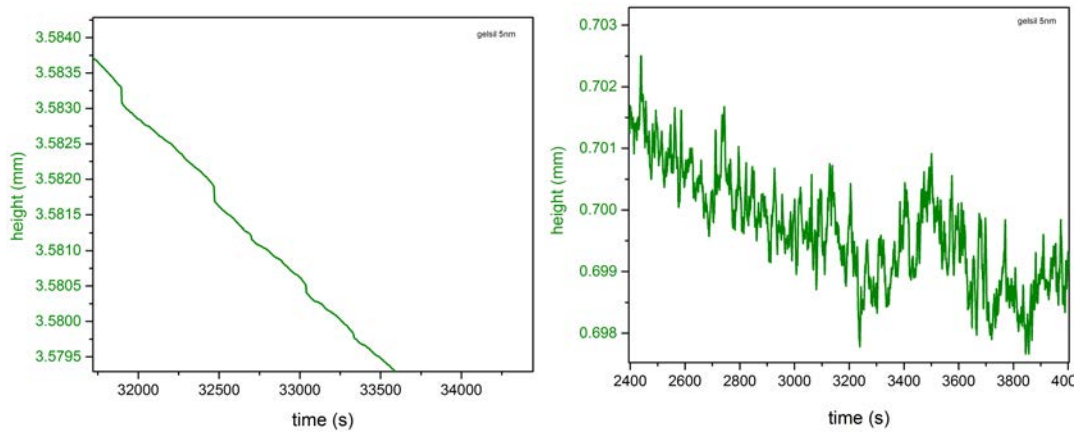


Figure 6.13: Gelsil 5: Changes of sample height under compression measured by Diamond DMA,  $R=40\text{mN/s}$  (left) and DMA 7e,  $R=60\text{mN/s}$  (right)



# 7 Analysis of data

## 7.1 First evaluation method - 'searching for power-laws in the wrong region'

When analyzing the data, it is most interesting to calculate the distributions for obtaining the exponent of the **maximum velocity distribution** and the exponent of the **maximum velocity squared distribution**. For these exponents either the absolute values of the velocities or the velocity squared values are used for calculation.

In case of a cycle measurement, each cycle can be examined individually (to compare the exponents of each) or all of them can be analyzed collectively after removing the large events due to the release of the force followed by increasing force at the start of the next cycle.

For the following evaluation example, the data for all cycles of the first Shale measurement was used. For all cycles all values of the absolute values of the velocity from 0 to approx. 195.000s (which is at the end of all cycles) were considered. After cropping the largest velocity values all positive velocity values were removed as well, because they correspond to backjumps and relaxation of the sample and only the negative values were used. Out of these, the absolute values were evaluated.

Then, using a 'peak analyzer' in Origin the number, position and values of the peaks in the spectrum were indentified with the Local Maximum method. To find local maxima, two neighbouring points were included [25].

## 7 Analysis of data

With the information of the peak positions (as absolute values of velocities) it is possible to plot a histogram<sup>1</sup> and thence establish a distribution curve. An example of such a histogram is depicted in figure 7.1 for the data of all cycles. The distribution of the peak velocity values is visible there.

To construct a histogram, Origin divides the data set of the velocity values into several sets (or intervals) of the same size and counts the number of values that happen to be in same data set [24]. This method is referred to as 'binning'. Therefore, the histogram shows the counts for each bin as function of the velocity values.

In order to get a smoother distribution, the 'bin size' can be changed manually.

In case of power-law distributions, logarithmic binning is usually used, since it has the advantage of reducing the number of zero and low count bins at larger velocity values [30].

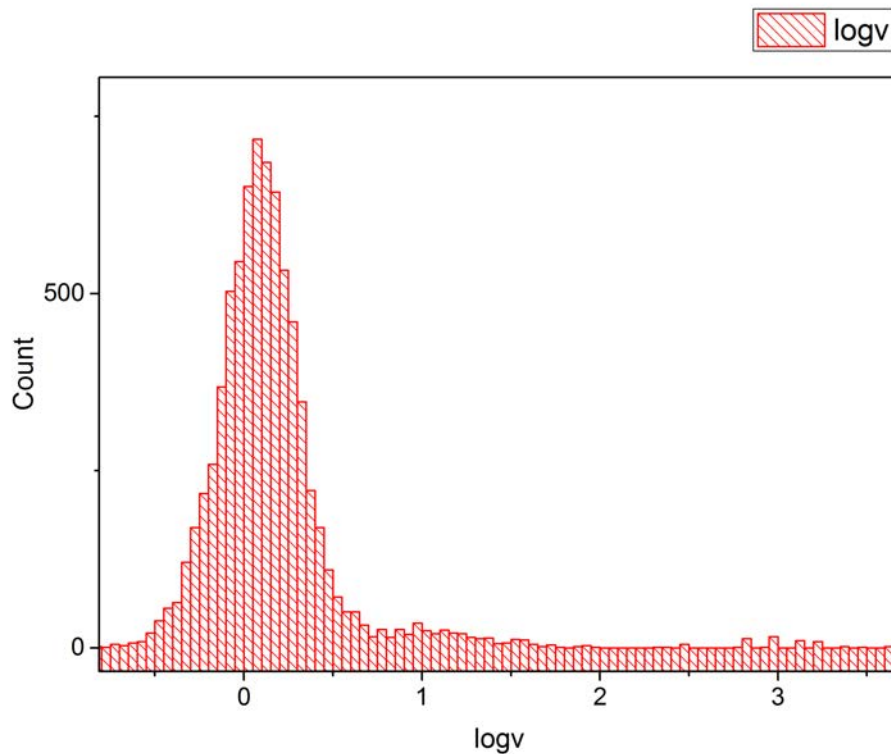


Figure 7.1: Shale 1: Histogram - shows the distribution of the absolute values of peak velocities, constant logarithmic bin width = 0.05 (Binning is done logarithmically)

<sup>1</sup>The histogram represents the frequency distribution of the absolute values of velocities in this case.

### 7.1 First evaluation method - 'searching for power-laws in the wrong region'

For further evaluation of the histograms, 'bin centers' (which are the velocity values at the center of each bin) are utilized for counting the number of events within each bin.

With these values, a distribution curve is plotted, as can be seen in figure 7.1 and 7.2. The corresponding power-law exponent is usually determined from a linear regression of a corresponding log-log plot.

If the diagram is plotted linearly the critical exponent  $\mu$  for the peak velocity distribution can be evaluated using a power-law in the form of  $N(v_m) \propto v_m^{-\mu}$ <sup>2</sup>, or in case of the maximum squared velocity distribution  $N(v_m^2) \propto (v_m^2)^{-\epsilon'}$ . As the velocity squared values are assumed to be proportional to the released energy  $E$  of the corresponding avalanches, and the counts  $N$  are proportional to probability  $P$ , this formula can also be written as  $P(E) \propto E^{-\epsilon'}$ .

In a log-log plot, this distribution corresponds to a straight line because taking the logarithm of this formula yields  $\ln[P(E)] \propto \epsilon' \ln(E) + constant$  [6].

It is, however, important to note, that such a procedure bears some pitfalls. One of them is that for logarithmic binning, the so determined power-law exponent is given by  $\epsilon' + 1$  instead of  $\epsilon'$ . (This logarithmic binning issue is well explained in a work of White et al. [32].) When beginning to conduct the experiments described in this thesis, the logarithmic binning problem was certainly an issue. As the exponents were determined incorrectly, the power-laws were searched for in the wrong region. Figure 7.2 shows an example of such an incorrect fitting procedure.

---

<sup>2</sup> $v_m$  denotes the maximum velocity values,  $N$  the number of events with a given velocity, i.e. the counts.

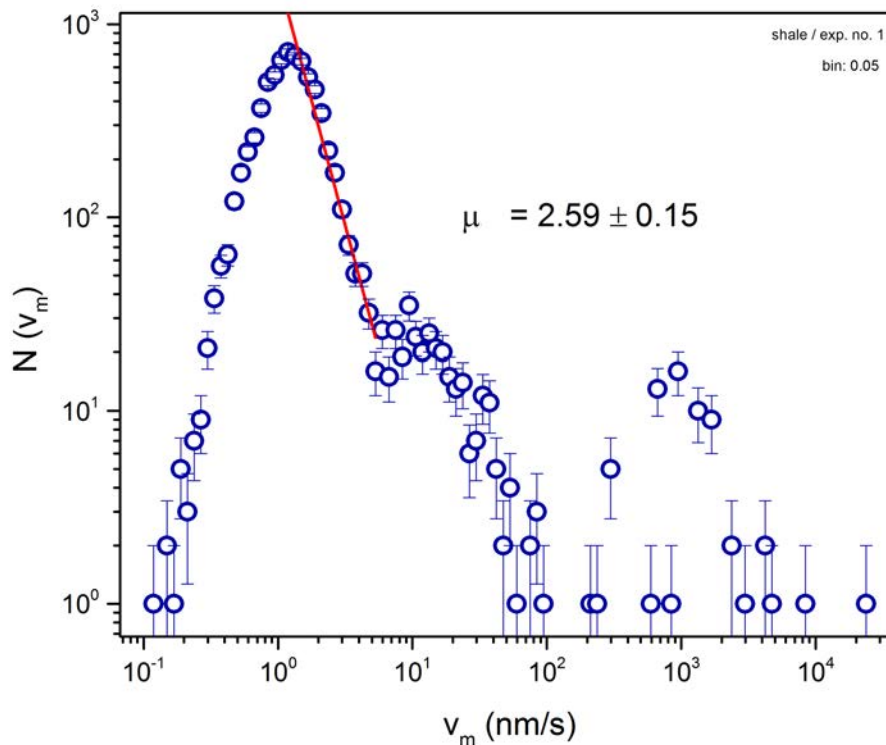


Figure 7.2: Shale 1: Maximum velocity distribution

Using this flawed evaluation method, the critical exponent of the maximum velocity distribution, labelled  $\mu$ , would yield for the first Shale measurement  $\mu = 2.59 \pm 0.15$ . It is visible that this fit does not show the expected power-law behaviour - it is not well defined over several orders of magnitude and is far too high for a maximum velocity distribution according to tabular 2.1.

Additional data points occur at high velocity values that cannot be included in the fit. When applying this flawed evaluation method to the other samples, similar incorrect results are obtained.

In the beginning of the experiments, the poor results of the power-laws were attributed to the DMA device, as the logarithmic binning issue had not been taken into account. Therefore, additional experiments were carried out using the DMA 7e, a far more accurately measuring device than the Diamond DMA. As a results, it appeared clear that little might be gained from using the DMA 7e, and the distribution curves did not satisfy power-law be-

haviors over several orders of magnitude, as indicated already in chapter 6.3. Therefore, the evaluation routine had to be questioned, and logarithmic binning was discovered to require a much more careful use.

## 7.2 New evaluation method - Logarithmic binning transformed to linear

As the first evaluation method resulted in incorrect exponents, a different new routine for analyzing the data was applied.

The logarithmic binning problem arises because of the logarithmic binning of the velocity and velocity squared values during the data evaluation to obtain a histogram. Logarithmic binning is used for plotting the histograms, because in case of a linear binning, many counts are at low values and the bin size cannot be set small enough to obtain enough counts at high values to construct a histogram. (This is due to the power-law distribution of the data.) This means that linear binning leads to a large number of zero and low count bins, especially at high values of  $v_m$  or  $v_m^2$ .

In power-law distributions, logarithmic binning reduces this number of zero and low count bins at larger  $x$  values, because the linear width of a bin increases linearly with  $x$  [32]:

$$w_i = x_i(e^b - 1) \quad (7.1)$$

$b$  being the constant logarithmic width:  $b = \log(x_{i+1}) - \log(x_i)$ .<sup>3</sup> Therefore, the number of counts for each bin depends not only on  $x$  but also on the linear width of the bin and, hence, the slope of the distribution curve is  $\epsilon + 1$  instead of  $\epsilon$ , which would be obtained for linear binning [32].

---

<sup>3</sup>In this reference  $\log$  is used for the natural logarithm. Therefore, when applying this formula to the logarithm to the base 10 the exponential function in equation 7.1 has to be replaced by 10.

## 7 Analysis of data

In order to deal with this problem the diagram is rescaled so that the slope of the distribution curve yields the exponent value of  $\epsilon$  even when logarithmic binning is used. The rescaling factor can be estimated with the identity:

$$P(\log(x))d\log(x) = P(x)dx \quad (7.2)$$

$$P(\log(x))\frac{dx}{x \cdot \ln(10)} = P(x)dx \quad (7.3)$$

$$\frac{P(\log(x))}{x \cdot \ln(10)} = P(x) \quad (7.4)$$

As the probability  $P$  is proportional to the Counts  $N$ , this rescaling factor can be used for rescaling the y-axis of the distribution curve obtained after drawing the histogram with Origin. In order for the units to be correct, a factor with the unit of  $x$  has to be multiplied on the left side of the equation.

In the following diagrams it has been accounted for this logarithmic binning error in defining  $N$  as [30]:

$$N(x) \equiv \hat{N}(\log_{10}x)/x \quad (7.5)$$

Another problem that occurred during the evaluation was the noise present in the data, an issue which was initially not taken into account, as the researchers had not been aware of the problem.

As an example, an older cycle measurement of Vycor (see measurement details in figure 6.7) is picked. With the wrong evaluation method, a distribution curve as depicted in figure 7.3<sup>4</sup> (logarithmic binning) was fitted with an exponent  $\epsilon' = 2.0 \pm 0.01$  using the formula  $N(v_m^2) \propto (v_m^2)^{-\epsilon'}$ . It can be seen in this diagram that everything on the left side of the peak was attributed to noise and the power-law was evaluated only using a small region on the right side of the peak.

---

<sup>4</sup>The label bin: 0.06 refers to the constant logarithmic bin width  $b$  of equation 7.1. In each of the following figures of the distribution curves the constant logarithmic width  $b$  is denoted in an analogous manner.

## 7.2 New evaluation method - Logarithmic binning transformed to linear

A closer inspection of the semi-logarithmic plot reveals quite a large tail at larger velocity values. It turns out that this tail contains the actual power-law information of the squared drop velocity distribution. Apart from the wrong fitting of the curve, the estimated slope of the curve is actually  $\epsilon + 1$  because logarithmic binning is used for drawing this distribution curve. This would give a slope of about  $\epsilon = 3$  which is too high compared to exponents estimated in previous work, e.g. [19], [23], [4]. Baró et al. estimated the exponent of the distribution of avalanche energies for Vycor to be about  $\epsilon \sim 1.4$  [4], as mentioned in chapter 3.2.

7 Analysis of data

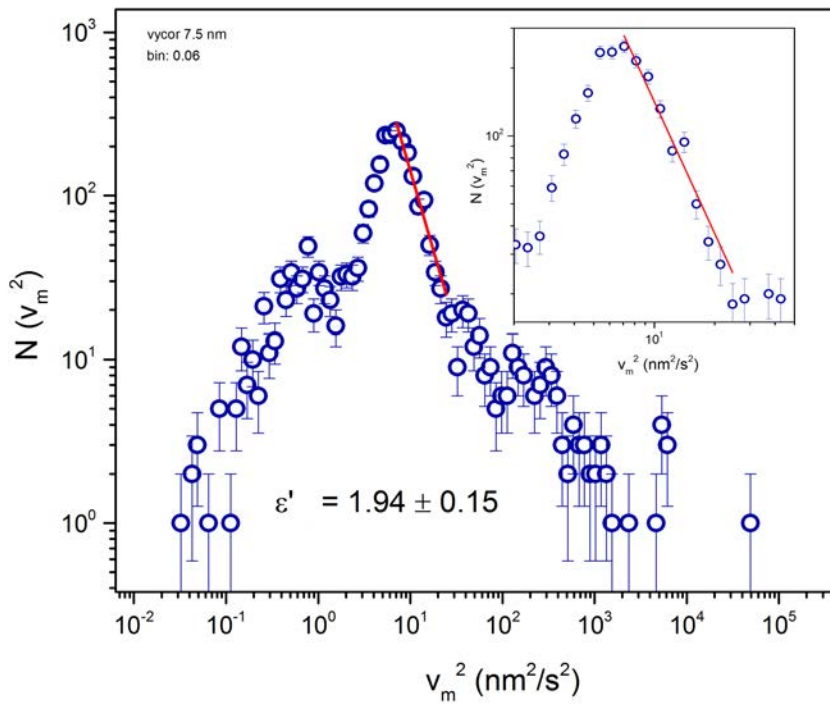
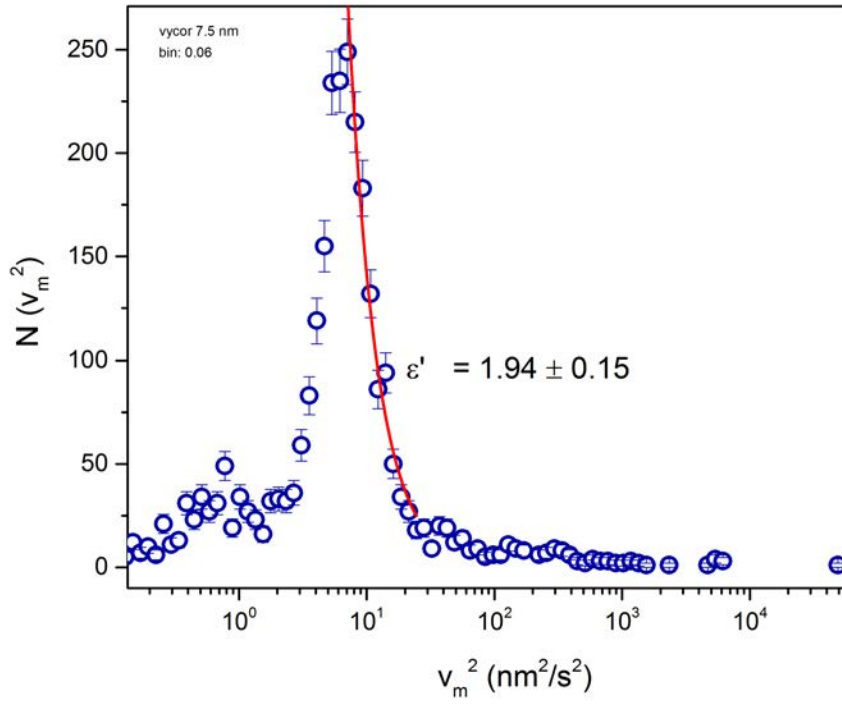


Figure 7.3: Vycor 7.5nm: Semi-logarithmic plot (upper figure) and log-log plot (lower image) of the (incorrectly evaluated) distribution of maximum drop velocity squared values; the inset shows a magnification of the fitted part in log-log scale (stress cycling measurement)

Figure 7.4 shows the diagram rescaled by dividing the Number of events  $N$  by the velocity squared values as shown in equation 7.5.

The rescaling of the y-axis reveals the behavior of the data hidden in the 'tail' of the semi-logarithmic plot, 7.3. This diagram demonstrates very clearly that for large velocity squared values one obtains a rather nice power-law behavior with an exponent of 1.41 that is stable for about three orders of magnitude.

In figure 7.4 a non-power-law region can be seen in the left part of the distribution curve. On the one hand, this could be due to noise from the DMA or due to overlapping a number of avalanches as a result of the poor time resolution of the DMA. On the other hand, it might also arise from smaller cracks appearing out of large cracks or even from cracks coming from the surface. This part at low velocity squared values do not yield a correct power-law exponent. In the old evaluation of figure 7.3 actually the right part of the non-power-law part of the distribution was fitted and, hence, the estimated exponent was incorrect and too high. Another indication for a flaw in the previously estimated exponent is that it was only valid in a narrow size range for merely about one order of magnitude.

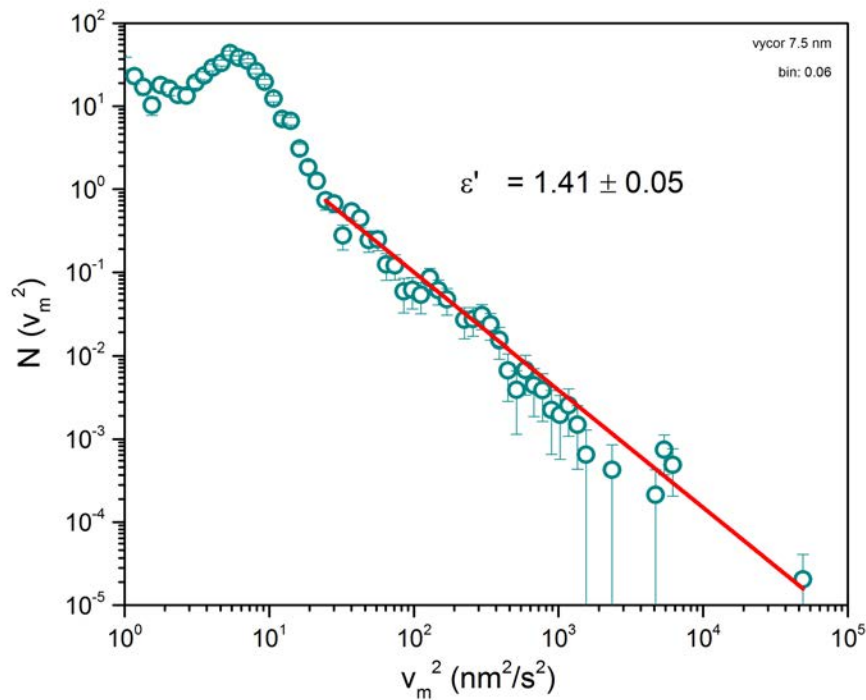


Figure 7.4: Vycor 7.5nm cycle measurement: Log-log plot of the distribution of maximum drop velocity squared values

## 7 Analysis of data

In order to examine whether this assumption about the actual power-law data being hidden in the 'tail' of the semi-logarithmic plot of the squared drop velocity distribution is correct, the number of aftershocks following a mainshock is plotted, see figure 7.5. The Omori's plot is obtained using the time when consecutive jerk events occur. This is done with a time bin, i.e. a histogram of the time of velocity squared peaks. For Omori's plot, the non-power-law part has to be removed from the data set, in order for the remaining data (which actually show power-law behavior) to reveal an Omori's law. For fitting the modified Omori's law for the number of aftershocks  $r_{AS}$  is used:

$$r_{AS}(t) = k \cdot (t + c)^{-p} \quad (7.6)$$

In this formula  $c$  denotes some constant,  $t$ =time and  $p$  the Omori's exponent [30]. The Omori's exponent was estimated to be approximately about  $p = 0.6$  for Vycor and Gelsil, figure 7.5. (Usually the exponent  $p$  is in the range of 0.6-1.)

This exponent corresponds perfectly well with the Omori's exponent of reference [4].

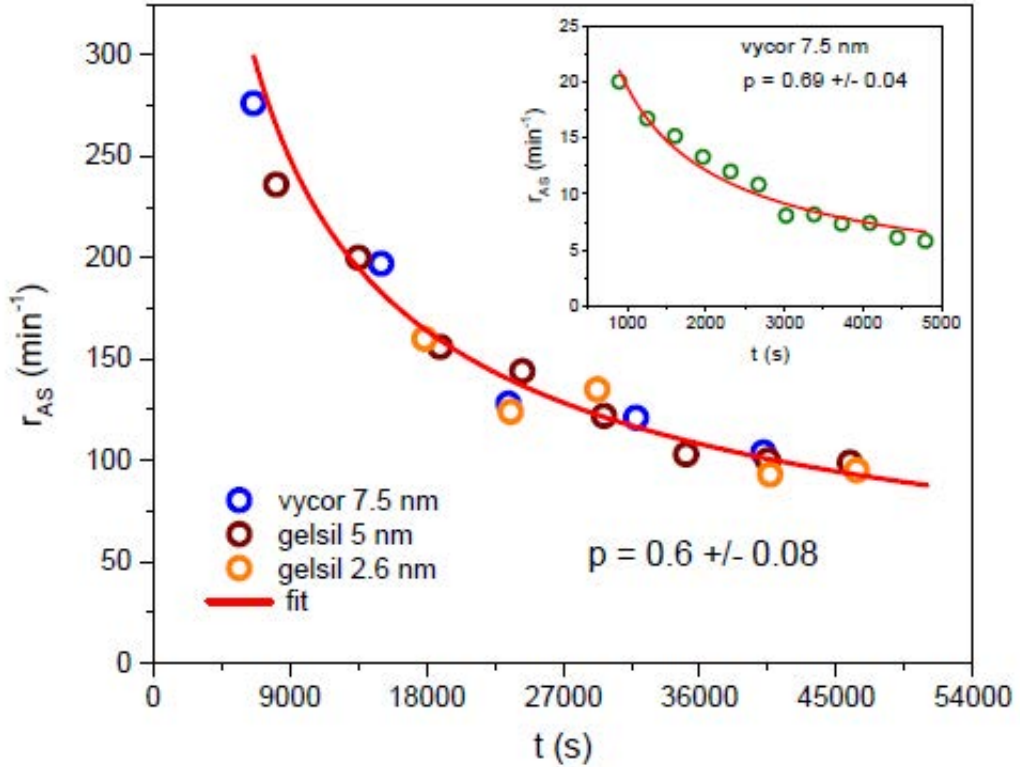
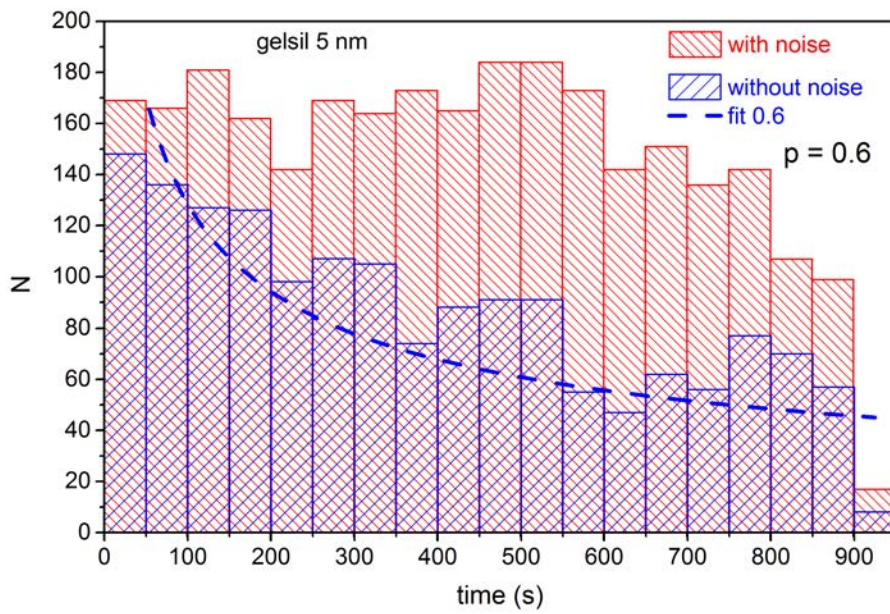


Figure 7.5: Number of aftershocks per unit time  $r_{AS}$  as a function of time distance to the main shock calculated from different long time experiments of Vycor and Gelsils. The red fit corresponds to Omori's law with  $c=0$  and  $p = 0.6 \pm 0.08$ . In the inset a stress cycle experiment of Vycor is depicted.

If the non-power-law part in the squared drop velocity distribution is not cut sufficiently, an equally distributed histogram in time instead of Omori's behavior of aftershocks is obtained. This was checked and evaluated for Gelsil 5nm, see figure 7.6. (This data set stems from an older Gelsil 5nm measurement, see figure 6.10.) It becomes clear that the shape of the time histogram changes considerably after cutting the non-power-law part and follows an Omori's law with exponent of about  $p = 0.6$ . Diagram 7.7 shows that the power-law part follows a nice Omori's law, as in the previous figure, and the inset shows only the non-power-law part, which does not follow any Omori's law.

7 Analysis of data



t = -16

Figure 7.6: Gelsil 5nm: Time histograms of the squared drop velocity events with and without non-power-law part present

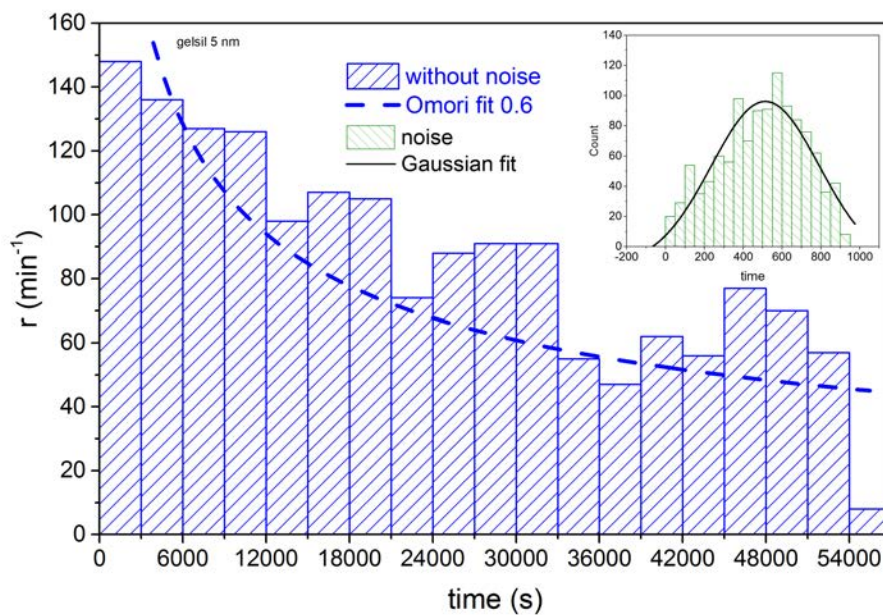


Figure 7.7: Gelsil 5nm: Time histogram of the squared drop velocity events without the non-power-law part, the inset shows the time histogram of the non-power-law part only

## 7.2 New evaluation method - Logarithmic binning transformed to linear

Figure 7.8 depicts the distribution curve for this Gelsil measurement done with the improved evaluation method. This curve yields a critical exponent of about 1.40 which is in comparatively good agreement with reference [23], see 3.3, they reported for their Gelsil 5 nm samples exponent values of  $1.35 \pm 0.03$  and  $1.37 \pm 0.03$ .

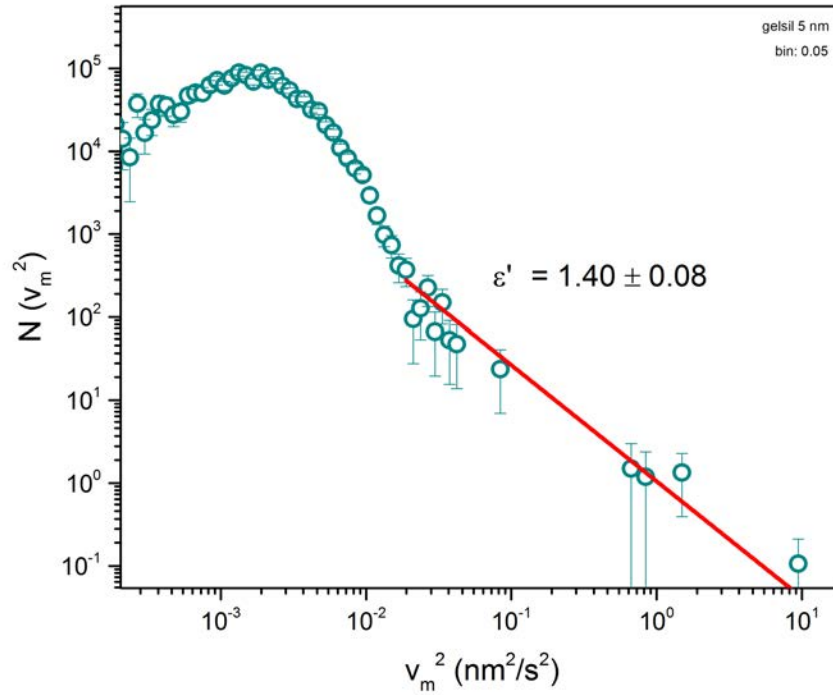


Figure 7.8: Gelsil 5nm: Log-log plot of the distribution of maximum drop velocity squared values.

Another measurement yielding a very good exponent value is an old Gelsil 2.6nm. The according distribution curve is depicted in figure 7.9 and is fitted with a power-law  $\epsilon' \approx 1.41$ . The inset reveals that this Gelsil sample was studied in a cycle measurement.

## 7 Analysis of data

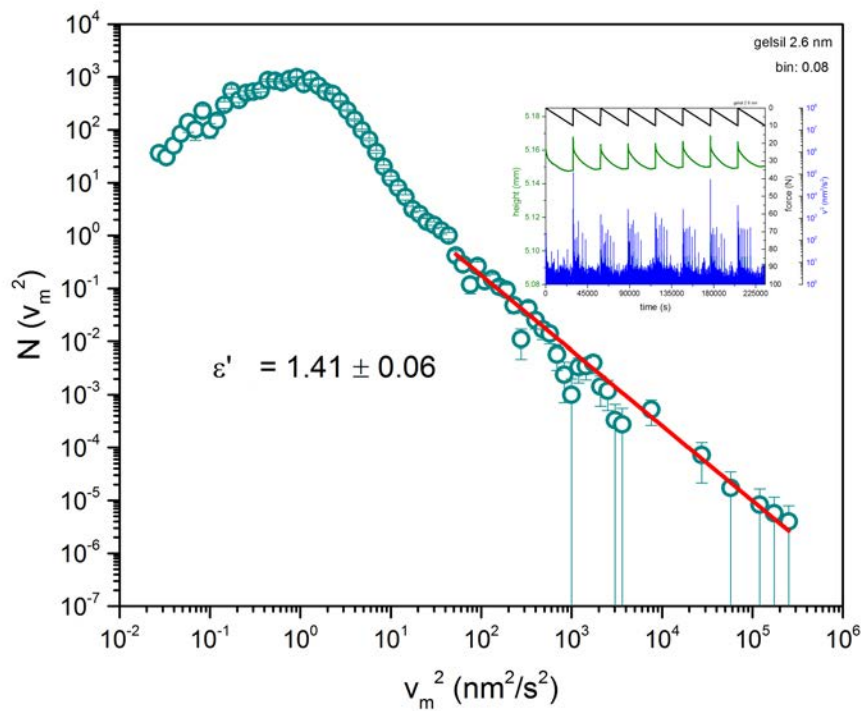


Figure 7.9: Gelsil 2.6: Log-log plot of the distribution of maximum drop velocity squared values, the inset shows the sample evolution, force and squared drop velocities during the measurement

These comparisons between the measurements carried out by DMA and the previously performed measurements with acoustic emission suggest a better agreement in critical exponents and the improved evaluation method appears to work rather accurately.

In the following, the results of applying this improved evaluation method to the measurements performed during the work is shown. For the fourth Shale measurement the distribution curve, in figure 7.10, can be fitted to obtain a power-law behaviour valid over several orders of magnitude.

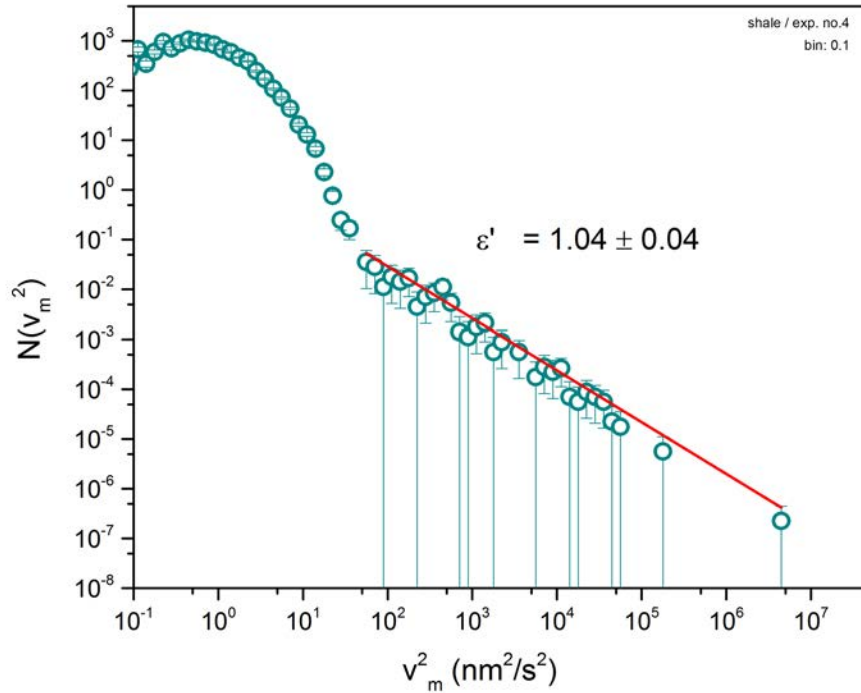


Figure 7.10: Shale 4: Maximum velocity squared distribution

The distribution curve for the first experiment on Shale, which was a short cycle measurement, is visible in figure 7.11. (Velocity squared values of all cycles were used for this distribution curve.) It shows a rather well defined power-law with exponent of 1.25, which is slightly higher than the exponent evaluated for the previous non-cycle measurement. Again the cycle measurement yields a far better defined power-law as the one stress ramp measurement. The individual cycles of this Shale measurement yield smaller exponent values when compared to considering the four cycles altogether: for cycle 1  $\epsilon' = 1.14 \pm 0.05$ , for cycle 2  $\epsilon' = 1.20 \pm 0.05$  and for cycle 3  $\epsilon' = 1.20 \pm 0.05$ . The power-laws for each individual cycle are not as well-defined as for all cycles together.

For the squared drop velocity exponent of Shale, a value similar to Vycor was expected, however, as no references for comparison exist, it might be argued that Shale behaves slightly differently than Gelsil and Vycor, as it has a different porous structure and is not a synthetic but rather a natural material.

## 7 Analysis of data

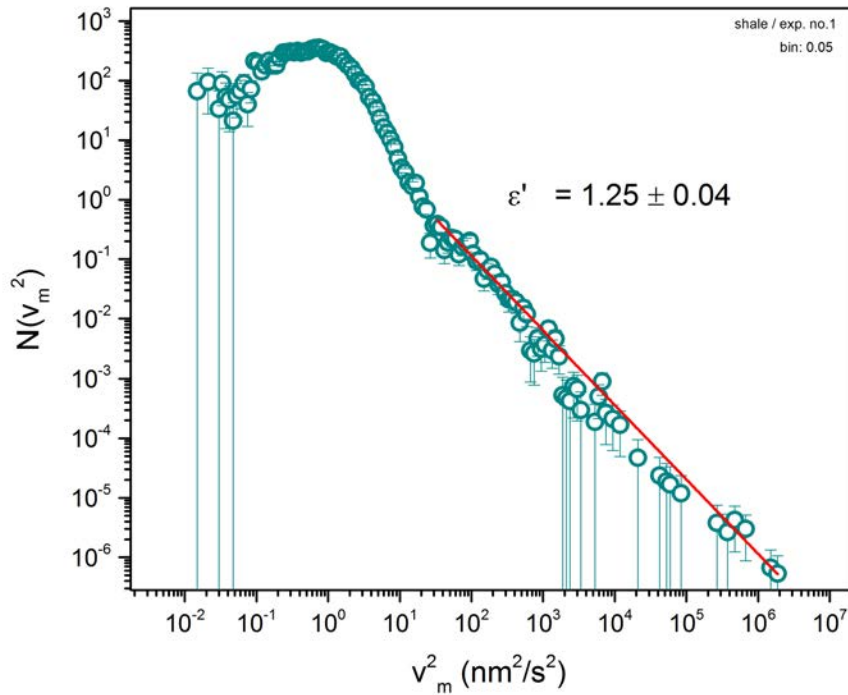


Figure 7.11: Shale 1: Maximum velocity squared distribution

Figure 7.12 shows the squared drop velocity distribution for a cycle measurement (see figure 6.8) of Gelsil 2.6nm. (Data points of all cycles were used to calculate this distribution curve.) A power-law is rather well defined, stable over several orders of magnitude with estimated exponent of about 1.58.

7.2 New evaluation method - Logarithmic binning transformed to linear

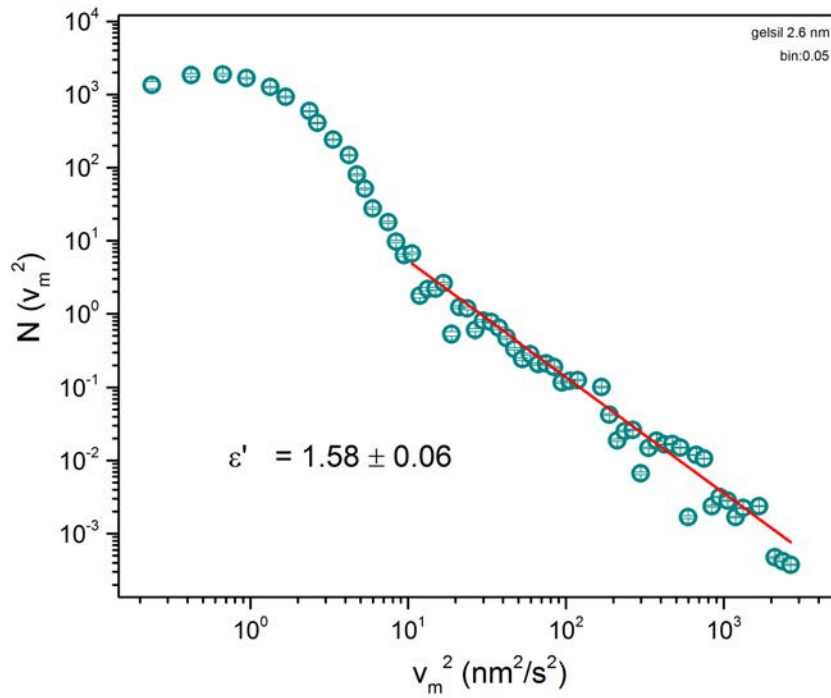


Figure 7.12: Gelsil 2.6nm: Maximum velocity squared distribution

As already suggested, the cycle measurements yielded the best estimates for exponent values and most stable and well defined power-laws. An example of a distribution curve of a one stress ramp measurement can be examined in figure 7.13. A power-law at high velocity squared values is more or less visible but not nicely defined.

## 7 Analysis of data

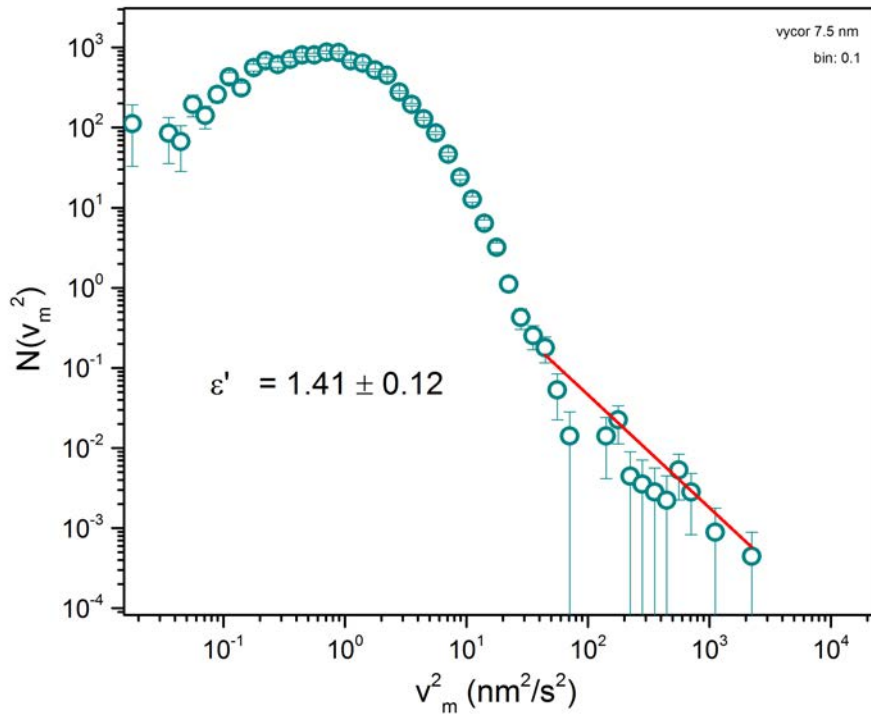


Figure 7.13: Vycor 7.5nm: Maximum velocity squared distribution

Regarding the maximum velocity distribution, three examples are shown in figure 7.14, figure 7.15 and figure 7.16 below. The exponent values are slightly lower than expected from mean-field-theory, see section 2.3, expect for the Gelsil 2.6 measurement.

7.2 New evaluation method - Logarithmic binning transformed to linear

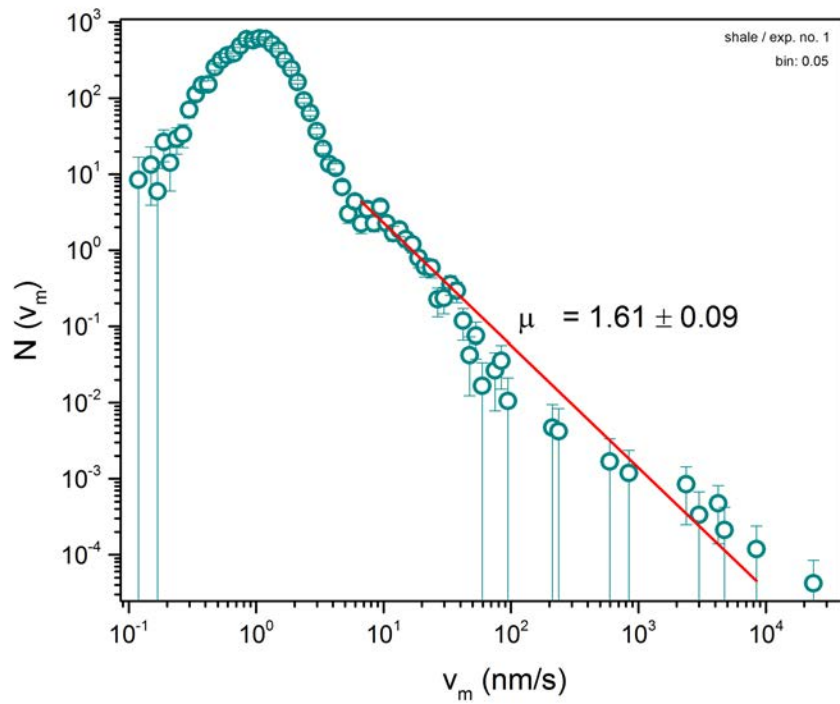


Figure 7.14: Shale 1: Maximum velocity distribution (short stress cycling measurement)

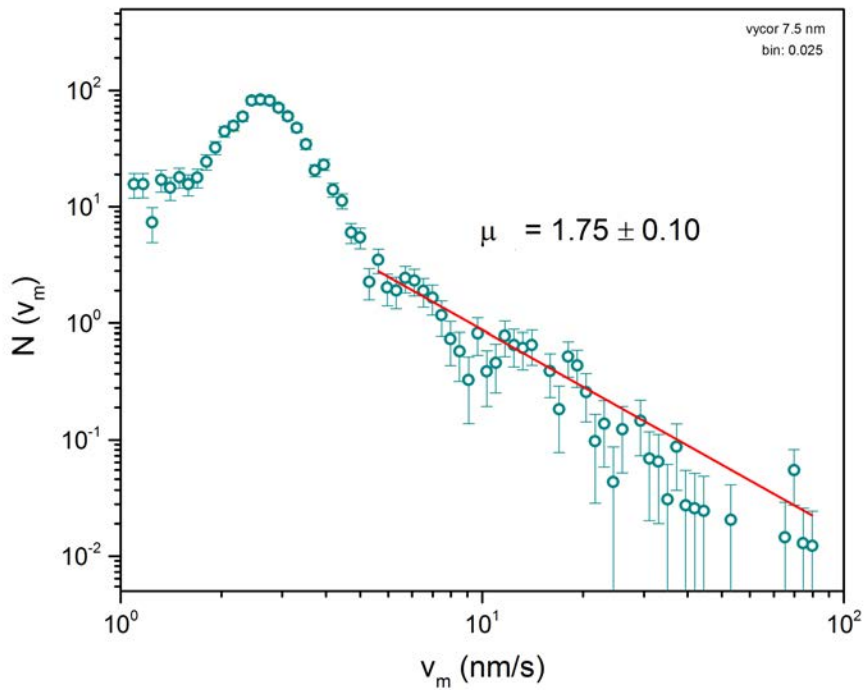


Figure 7.15: Vycor 7.5nm: Maximum velocity distribution (stress cycling measurement)

## 7 Analysis of data

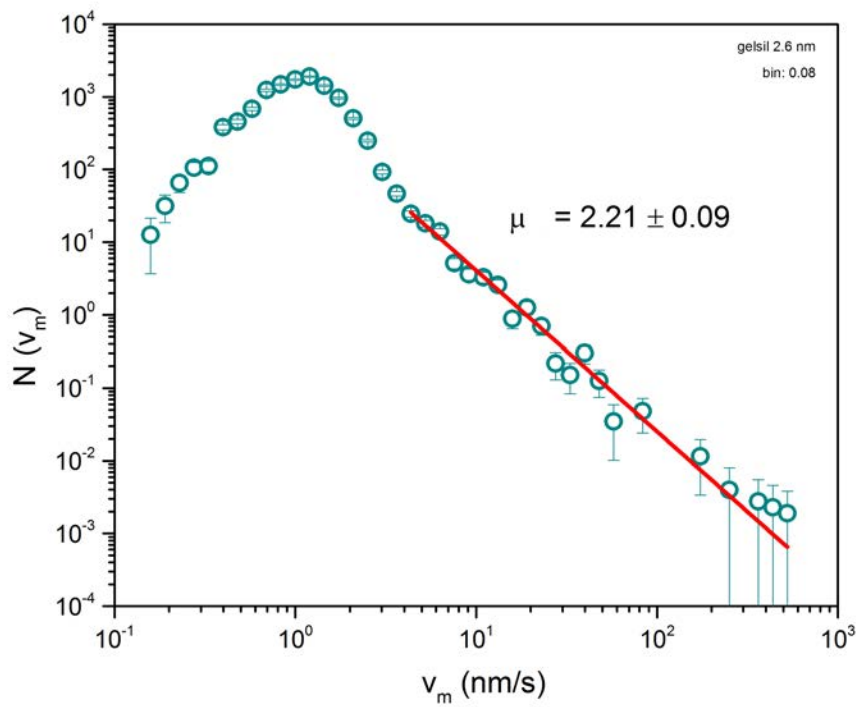


Figure 7.16: Gelsil 2.6nm: Maximum velocity distribution (stress cycling measurement)

Altogether, it can be concluded that the results of the DMA measurements are in good agreement with the AE experiments. Acoustic emission experiments, on the one hand, yield an energy exponent of about  $\epsilon = 1.39$  (e.g. [4]), which is consistent with the mean-field value of  $\epsilon = 1.33$  (see tabular 2.1). Concerning the DMA measurements, on the other hand, the exponent of the squared drop velocity distribution  $N(v_m^2)$  is estimated to be not too far from  $\epsilon' = 1.5$  (for Gelsil and Vycor) which corresponds rather well with the mean-field value of  $\epsilon' = 1.5$  (see tabular 2.1).

# 8 Acoustic emission data for Vycor

## 7.5nm

In a study of Nataf et al. [23] not only the acoustic emission activities were measured, but also the jerky changes of samples height, using a laser extensometer with a nominal resolution of 100nm. The squared drop velocities (calculated from the sample deformation) as function of time were reported to correspond rather well with the measured acoustic emission activities, as shown in figure 3.6. In order to learn more about the correspondence between the AE activities and the calculated squared drop velocities, an example of an AE measurement was analyzed.

An original data set from a previous study of Vycor done by Baró et al. [4] was requested in order to compare the AE activities to the squared drop velocities. The data are from a Vycor experiment performed under uniaxial compression with simultaneously measuring the evolution of the sample height and the acoustic emission activities.

The time resolution of AE experiments is some orders of magnitude better than DMA experiments, as usually AE is done in the range of MHz. The AE data of Vycor were cumulated every 10ms.

Figure 8.1 suggests a good correspondence between the acoustic emission activities and the squared drop velocities. For further calculation of the energy distribution, energy signals below 0.5aJ have been discarded to reduce noise.

8 Acoustic emission data for Vycor 7.5nm

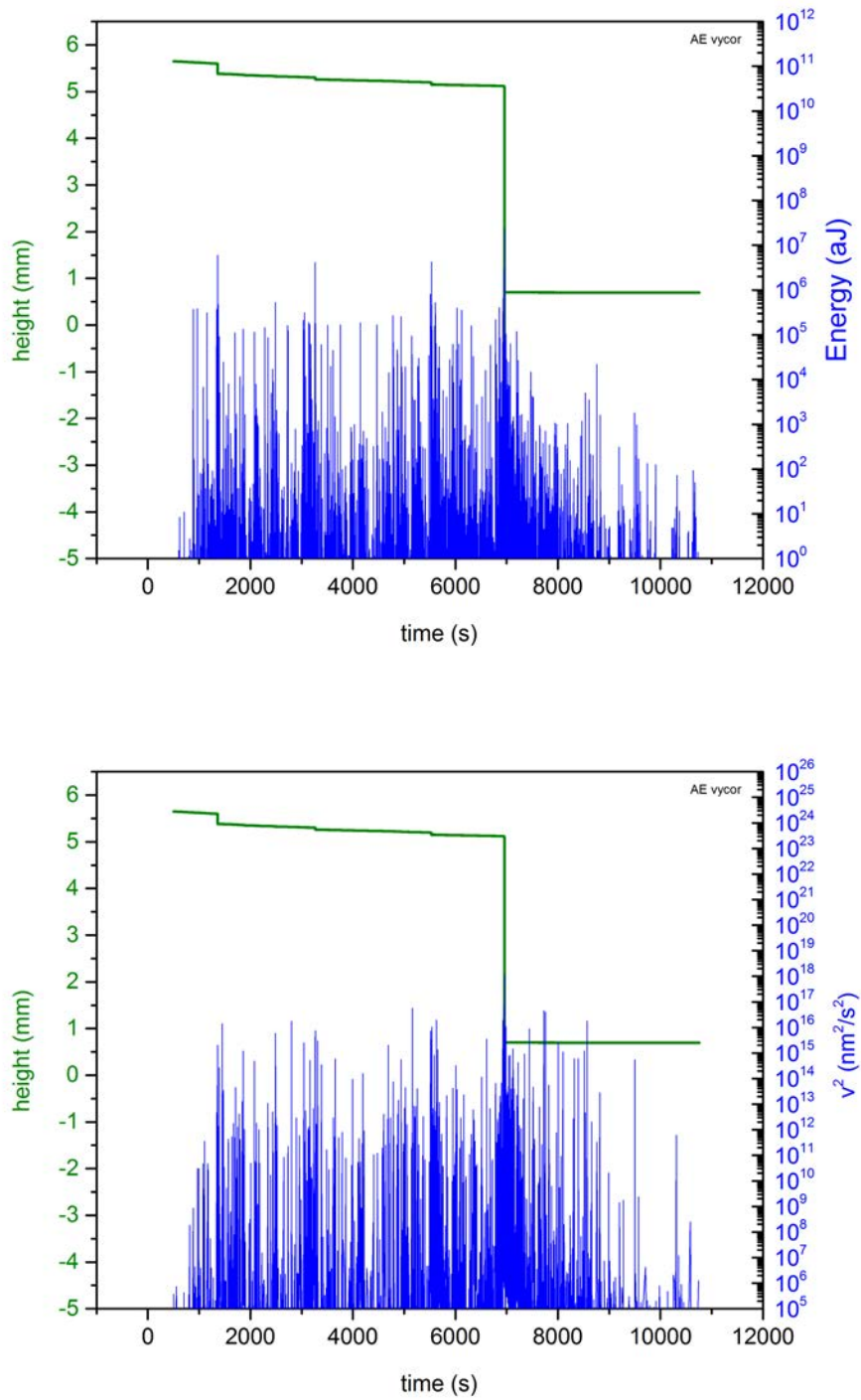


Figure 8.1: AE Vycor: Evolution of the sample height (green) and acoustic emission activities (blue) - upper figure - and accordingly square drop velocities (blue) - lower figure - as functions of time

Figure 8.2 represents how the energy distribution of the acoustic emission signals can be fitted with a power-law of exponent 1.37. This power-law is stable over more than six orders of magnitude and shows that even for time cumulated energy values the exponent is rather stable and close to the expected value of 1.39, as evaluated by Baró et al., compare figure 3.4. This distribution curve is obtained via logarithmic binning of the cumulated energy values, after discarding signals below 0.5aJ. (Besides, the correct power-law behavior indicates that the improved evaluation method considering the logarithmic binning problem and the compensation of this error by rescaling the y-axis is indeed correct.)

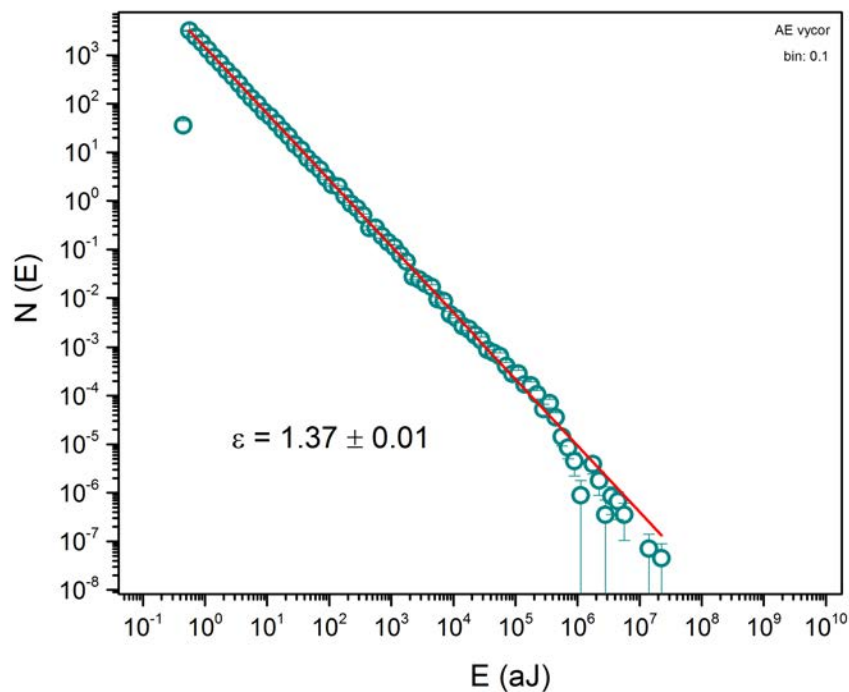


Figure 8.2: AE Vycor: Energy distribution of acoustic emission events (with the improved evaluation method)

The squared drop velocity distribution as shown in figure 8.3, is calculated from the measured sample height during their acoustic emission experiment. For this distribution curve the local maximum method was not used to find local velocity squared maxima, but a histogram is plotted with logarithmized velocity squared values. For drawing the distribution curve, again, the logarithmic binning error is taken into account.

## 8 Acoustic emission data for Vycor 7.5nm

The distribution curve appears to have a flat kink and fitting the curve as a whole would lead to a rather low exponent of about 1. Only considering a part of the curve at high velocity squared values, a power-law with exponent 1.36 can be fitted. This exponent value corresponds very nicely with the estimated exponent of the acoustic emission energy distribution, figure 8.2. Apparently, measuring the sample height with a laser extensometer with a resolution of about  $100nm$  also yields quite well results.

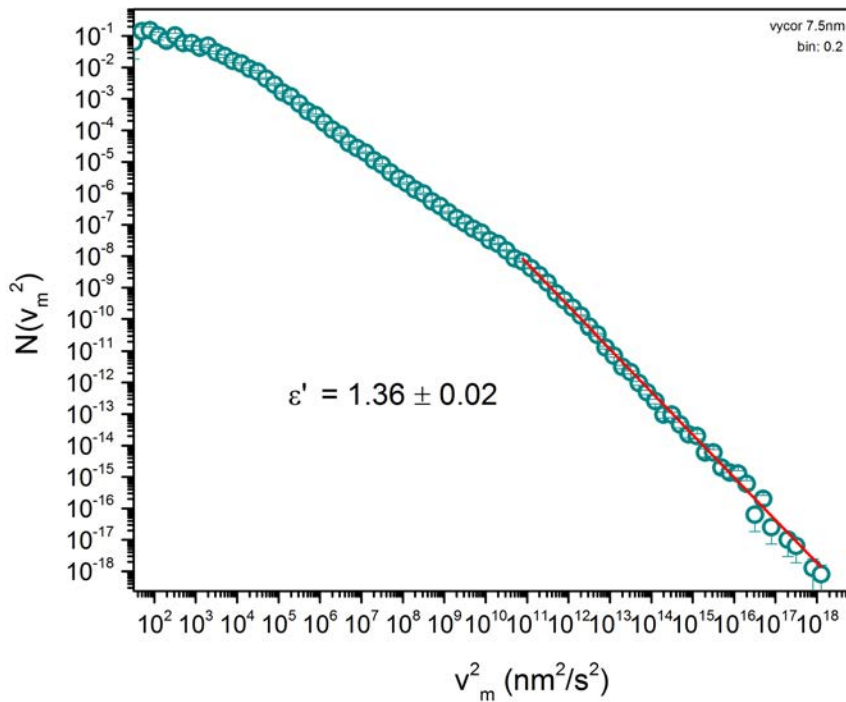


Figure 8.3: AE Vycor: Maximum squared drop velocity distribution (with the improved evaluation method)

## 9 Conclusion

This thesis presents an analysis of crackling behavior of nanoporous materials in slow uniaxial compression experiments with the help of a recently developed measurement technique [30]. This new method includes measuring the evolution of the sample height and correlating the changes of height under compression to the elastic strain energy released upon sample deformation.

The measurements were carried out with very low compression rates in the range of  $0.1mN/s - 10mN/s$  with a DMA. The sample deformed due to the applied external stress in a sequence of jerky events and avalanches. These result from breaking of nanometer-scaled pores (Vycor: 7.5nm, Gelsil: 2.6nm and 5nm). With the statistical information about the velocities corresponding to the jerky changes in sample height, the statistics of these crackling events were investigated. In doing so, distribution curves were calculated as the maximum drop velocity squared distribution, and their scaling behavior was analysed.

It was discovered that critical exponents of distributions, like the maximum squared drop velocities  $D(v_m^2) \sim (v_m^2)^{-\epsilon'}$  and the maximum drop velocities  $D(v_m) \sim (v_m)^{-\mu}$ , hold for more than three orders of magnitude and are even in good agreement with the expected exponent values estimated by mean-field-theory ([26], [23]). Additionally, the exponents showed good correspondence with the exponents from acoustic emission experiments ([27], [4]), although acoustic emission is a much more mature and precise measurement technique.

The main drawback of the DMA method is its poor time resolution of about  $1s$ , however, the DMA is able to apply the force uniformly with a resolution of  $2mN$  and the changes in sample height can be measured rather precise with an accuracy of about  $10nm$ .

## 9 Conclusion

For these experiments, much smaller samples than those used in acoustic emission experiments had to be prepared, because this specific DMA (Diamond DMA, PerkinElmer) used for measurements during this work is restricted to applying a force of  $10N$ .

For a more precise and comprehensive investigation using the DMA method, it is possible to switch to another DMA device, which is able to apply a larger stress and to increase the sampling rate. The samples have to be prepared as small as possible so that the available applied stress is high enough for macroscopic failure to be achievable in the porous samples.

Nevertheless, once these drawbacks of the DMA method can be eliminated, it presents a new possibility to analyze failure dynamics in nanoporous materials. Therefore, it might eventually become a sufficient alternative tool to acoustic emission experiments, especially when it comes to investigating crackling behavior under different conditions, for example at high temperatures.

# Bibliography

- [1] P Bak. Self-organized criticality. *Physica A: Statistical Mechanics and its Applications*, 163(1):403-409, 1990.
- [2] P. Bak. *How nature works: the science of self-organized criticality*. Springer Verlag, New York, 1996.
- [3] P Bak, C Tang, and K Wiesenfeld. Self-organized criticality. *Physical Review A* 38(1):364-374, 1988.
- [4] J. Baro, A Corral, X. Illa, A. Planes, E. K. H. Salje, W. Schranz, D. E. Soto-Parra, and E. Vives. Statistical similarity between the compression of a porous material and earthquakes. *Physical Review Letters*, 110(8):088702, 2013.
- [5] P. M. Chaikin and T. C. Lubensky. *Principles of condensed matter physics*. Cambridge University Press, Great Britain, 1995.
- [6] A. Clauset, R. Shalizi, and M. E. J. Newman. Power-law distributions in empirical data. *SIAM Review*, 51(4):661-703, 2009.
- [7] T. H. Elmer. *Engineered Materials Handbook 4, Ceramic and Glasses*. ASM International, Ohio, USA, 1992.
- [8] M. E. Fisher. The theory of equilibrium critical phenomena. *Reports on Progress in Physics* 30(2):615-730, 1967.
- [9] A. Ghaffar. *Confinement-Induced Structural Changes of Alkali Metals in Nanoporous Systems*. University of Vienna, Vienna, 2014.
- [10] J.T. Greensmith. *Petrology of the sedimentary rocks*. Unwin Hyman Ltd, London, UK, 1989.

## Bibliography

- [11] S. Hergarten. *Self-Organized Criticality in Earth Systems*. Springer Verlag, Berlin, Heidelberg, 2002.
- [12] M. Huang, L. Jiang, P. Liaw, C. R. Brooks, R. Seeley, and D. L. Klarstrom. Using acoustic emission in fatigue and fracture materials research. <http://www.tms.org/pubs/journals/JOM/9811/Huang/Huang-9811.html> accessed: 2015-11-26.
- [13] SII NanoTechnology Inc. *Pyris Diamond DMA - Dynamic Mechanical Analyzer (Instrument Manual)*. SII NanoTechnology Inc., 2003, Document no. 0503-511-088E.
- [14] R. L. Ingram. Fissility of mudrocks. *Bulletin of the geological society of america*, 1963; Vol.64; PP. 869-878.
- [15] H. Kanamori and E. E. Brodsky. The physics of earthquakes. *Reports on Progress in Physics* 67:1429-1496, 2004.
- [16] J. Koppensteiner. *The glass transition in nanoscaled confinement probed by dynamic mechanical spectroscopy*. University of vienna, Vienna, 2009.
- [17] J. Koppensteiner, Schranz W., and M. A. Carpenter. Revealing the pure confinement effect in glass-forming liquids by dynamic mechanical analysis. *Physical Review B* 81, 024202, 2010.
- [18] G. Krey. *Phasenuebergaenge und kritische Phaenomene*. Vieweg, Braunschweig, Wiesbaden, 1980.
- [19] M. LeBlanc, L. Angheluta, K. Dahmen, and N. Goldenfeld. Universal fluctuations and extreme statistics of avalanches near the depinning transition. *Physical Review E*, 87(2):022126, 2013.
- [20] Buehler Ltd. *IsoMet Low Speed Saw - Precision sectioning saw*. Buehler, Illinois, USA, 2005. 25M0305 FN00874 Rev. 2.
- [21] Buehler Ltd. *IsoMet Low Speed Saw - Precision sectioning saw*. Buehler, Illinois, USA, 2013. FN00874 1013.
- [22] K. P. Menhard. *Dynamical Mechanical Analysis - A Practical Introduction*. CRC Press LLC, Boca Raton, Florida, 1999.

- [23] G. F. Nataf, P. O. Castillo-Villa, J. Baro, X. Illa, E. Vives, A. Planes, and Ek. K. H. Salje. Avalanches in compressed porous  $\text{SiO}_2$ -based materials. *Physical Review E*, 90(2):022405, 2014.
- [24] Origin. Histogram. <http://www.originlab.com/doc/Origin-Help/Create-Histogram>, accessed: 2015-11-03.
- [25] Origin. Peak analyzer. <http://www.originlab.com/doc/Origin-Help/PeakAnalyzer-FindPeaks>, accessed: 2015-11-02.
- [26] E. K. H. Salje and K.A. Dahmen. Crackling noise in disordered materials. *Annual Review Condensed Matter Physics* 5:233-54, 2014.
- [27] E. K. H. Salje, D. E. Soto-Parra, A. Planes, E. Vives, M. Reinecker, and W. Schranz. Failure mechanism in porous materials under compression: crackling noise in mesoporous  $\text{SiO}_2$ . *Philosophical Magazine Letters*, 91(8):554-560, 2011.
- [28] J. P. Sethna. *Entropy, Order Parameters, and Complexity*. Clarendon Press, Oxford, UK, 2011.
- [29] J. P. Sethna, K. A. Dahmen, and C. R. Myers. Crackling noise. *Nature*, 410(6825):242-250, 2001.
- [30] V. Soprunyuk, S. Puchberger, W. Schranz, A. Tröster, E. Vives, and E. K. H. Salje. Towards a quantitative analysis of crackling noise by strain drop measurements. *Springerbook: Avalanches in functional materials and geophysics; E. Salje, A. Saxena, A. Planes; submitted*, 2016.
- [31] T. Utsu, Y. Ogata, and R. S. Matsu'ura. The centenary of the omori formula for a decay law of aftershock activity. *Journal of physics of the earth*, 43(1):1-33, 1995.
- [32] E. P. White, B. J. Enquist, and J. L. Green. On estimating the exponent of power-law frequency distributions. *Ecology*, 89(4):905-12, 2008.



# List of Figures

2.1	Histogram of the number of earthquakes in 1995 as a function of their magnitude [28] . . . . .	13
3.1	AE activity and deformation (at a stress of 1.6kPa/s) of the sample as function of time, inset: low AE activity in the initial part of the experiment [27] .	23
3.2	Energy distribution of the acoustic emission signals plotted in a log-log-plot. The four curves correspond to four different measurements using different compression rates. The power law exponent of $-1.39$ is represented by the dashed line [27]. . . . .	24
3.3	AE avalanche energy and change in sample height for a compression experiment with compression rate of $1.6kPa/s$ as functions of time [4]. . . . .	25
3.4	Avalanche energy distribution of the experiment with a compression rate of $1.6kPa/s$ and during 7 different subperiods. The straight line represents a power-law with exponent of $1.39$ [4]. . . . .	25
3.5	Number of aftershocks per unit of time as function of time difference to the mainshock. The dashed line represents Omori's law with exponent of $-0.75$ . The legend in each panel shows how the mainshocks are defined [4].	26
3.6	Gelsil 2.6 - (a) Sample height, (b) square of its time derivative, (c) AE activity [23] . . . . .	28
3.7	Log-log plot of energy distribution of AE events: from top to bottom curves correspond to Vycor, Gelsil 5nm, Gelsil 2.6nm, Light-gray sandstone, red sandstone and yellow sandstone, respectively. All curves, except for Vycor, are shifted for clarity [23] . . . . .	29
4.1	Fixture of the sample in a parallel plate setup in the <i>Perkin Elmer Diamond DMA</i> . . . . .	34
4.2	Dimensions of the sample in the parallel plate fixture . . . . .	34

*List of Figures*

5.1	Shale stones used for sample preparation . . . . .	38
5.2	Gelsil used for sample preparation [16] . . . . .	39
5.3	Comparison between the porous mesostructures of Gelsil (left) and Vycor (right) [16] . . . . .	40
5.4	Geometry of a typical compression experiment of a porous material using a DMA [30] . . . . .	41
5.5	Tools and utilities used for sample preparation . . . . .	42
6.1	Shale 1: Sample height (green), applied force (black) and squared drop velocities (blue) as functions of time (measured with Diamond DMA) . . .	46
6.2	Sample height as function of time for the first cycle from measurement time of 0 to 58000s, inset: magnification of a selected area of the plotted curve (measured with Diamond DMA) . . . . .	47
6.3	Shale 2: Sample height (green), applied force (black) and squared drop velocities (blue) as functions of time (measured with Diamond DMA) . . .	48
6.4	Shale 3: Sample height (green), applied force (black) and squared drop velocities (blue) as functions of time (measured with Diamond DMA) . . .	49
6.5	Shale 4: Sample height (green), applied force (black) and squared drop velocities (blue) as functions of time (measured with Diamond DMA) . . .	50
6.6	Vycor 7.5nm: Sample height (green), applied force (black) and squared drop velocity (blue) as functions of time (measured with Diamond DMA) .	51
6.7	Vycor 7.5nm: Sample height (green), applied force (black) and squared drop velocity (blue) as functions of time (measured with Diamond DMA), (With a y-axis break from 0.12mm-0.6mm the evolution of the sample is better displayed.) . . . . .	52
6.8	Gelsil 2.6: Sample height (green), applied force (black) and squared drop velocity (blue) as functions of time (measured with Diamond DMA) . . . .	55
6.9	Gelsil 5: Sample height (green), applied force (black) and squared drop velocities (blue) as functions of time (measured with Diamond DMA), (With a y-axis break from 1.8mm-3.5mm the evolution of the sample is better displayed.) . . . . .	56
6.10	Gelsil 5: Sample height (green), applied force (black) and squared drop velocities (blue) as functions of time (measured with Diamond DMA) . . .	57

6.11	Gelsil 2.6: Sample height (green), applied force (black) and squared drop velocities (blue) as functions of time (measured with DMA 7e) . . . . .	58
6.12	Gelsil 2.6: Changes of sample height under compression measured by Diamond DMA, R=40mN/s (left) and DMA 7e, R=200mN/s (right) . . . . .	59
6.13	Gelsil 5: Changes of sample height under compression measured by Diamond DMA, R=40mN/s (left) and DMA 7e, R=60mN/s (right) . . . . .	59
7.1	Shale 1: Histogram - shows the distribution of the absolute values of peak velocities, constant logarithmic bin width = 0.05 (Binning is done logarithmically) . . . . .	62
7.2	Shale 1: Maximum velocity distribution . . . . .	64
7.3	Vycor 7.5nm: Semi-logarithmic plot (upper figure) and log-log plot (lower image) of the (incorrectly evaluated) distribution of maximum drop velocity squared values; the inset shows a magnification of the fitted part in log-log scale (stress cycling measurement) . . . . .	68
7.4	Vycor 7.5nm cycle measurement: Log-log plot of the distribution of maximum drop velocity squared values . . . . .	69
7.5	Number of aftershocks per unit time $r_{AS}$ as a function of time distance to the main shock calculated from different long time experiments of Vycor and Gelsils. The red fit corresponds to Omori's law with $c=0$ and $p = 0.6 \pm 0.08$ . In the inset a stress cycle experiment of Vycor is depicted. . . . .	71
7.6	Gelsil 5nm: Time histograms of the squared drop velocity events with and without non-power-law part present . . . . .	72
7.7	Gelsil 5nm: Time histogram of the squared drop velocity events without the non-power-law part, the inset shows the time histogram of the non-power-law part only . . . . .	72
7.8	Gelsil 5nm: Log-log plot of the distribution of maximum drop velocity squared values. . . . .	73
7.9	Gelsil 2.6: Log-log plot of the distribution of maximum drop velocity squared values, the inset shows the sample evolution, force and squared drop velocities during the measurement . . . . .	74
7.10	Shale 4: Maximum velocity squared distribution . . . . .	75
7.11	Shale 1: Maximum velocity squared distribution . . . . .	76

*List of Figures*

7.12	Gelsil 2.6nm: Maximum velocity squared distribution . . . . .	77
7.13	Vycor 7.5nm: Maximum velocity squared distribution . . . . .	78
7.14	Shale 1: Maximum velocity distribution (short stress cycling measurement)	79
7.15	Vycor 7.5nm: Maximum velocity distribution (stress cycling measurement)	79
7.16	Gelsil 2.6nm: Maximum velocity distribution (stress cycling measurement)	80
8.1	AE Vycor: Evolution of the sample height (green) and acoustic emission activities (blue) - upper figure - and accordingly square drop velocities (blue) - lower figure - as functions of time . . . . .	82
8.2	AE Vycor: Energy distribution of acoustic emission events (with the improved evaluation method) . . . . .	83
8.3	AE Vycor: Maximum squared drop velocity distribution (with the improved evaluation method) . . . . .	84

# List of Tables

2.1	Selected exponent values predicted by MFT [26] . . . . .	18
3.1	Critical Exponents fitted for the different Gelsil samples [23] and for Vycor [4]	29
5.1	Characteristics of the studied Gelsil and Vycor samples according to refs [9], [17] . . . . .	40
6.1	List of Shale samples including their heights and cross sections . . . . .	44
6.2	Measurement settings for the Shale samples of tabular 6.1 . . . . .	44
6.3	Vycor sample including its height and cross section . . . . .	50
6.4	Measurement settings for the Vycor sample of tabular 6.3 . . . . .	50
6.5	List of Gelsil samples including their void size, height and cross section . .	53
6.6	Measurement settings for the Gelsil samples of tabular 6.5 . . . . .	54



# Abstract

This master thesis investigates the concept of crackling in nanoporous materials (especially Gelsil and Vycor, both  $\text{SiO}_2$ -based synthetic materials).

In this case, crackling refers to a jerky response of a system to changing external conditions like a driving force. The disturbance of the system through external forces results in impulsive events (avalanches) of a variety of sizes. Crackling events can occur in different systems ranging from crumpling pieces of paper to earthquakes and it has been discovered that many of those systems exhibiting crackling events show similar power-law statistics [26]. In the case of porous materials crackling can be observed when the material is compressed and avalanches occur due to the correlated nanometer-scaled pore breaking. Recent studies (e.g. [4], [27], [23]) on selected porous materials have shown that this behavior can be analyzed by applying a compressive force on the sample and simultaneously measuring the acoustic emission (AE).

The main task during the work on this thesis was to analyse and introduce a new method for studying crackling in porous materials [30]. This new method included experiments performed with a Dynamic mechanical analyzer (DMA), which was responsible for both applying a compressive force rather slowly in rates of  $0.1\text{mN/s} - 10\text{mN/s}$  and measuring the sample deformation. It was of utmost importance to find out whether similar power-law behaviors of the avalanche statistics as in AE experiments can be obtained by measuring the jerky evolution of the sample height.

It was discovered that critical exponents of such avalanche distributions hold for more than three orders of magnitude and are even in good agreement with the expected exponent values estimated by mean-field-theory. Additionally, the exponents showed good correspondence with the exponents from AE experiments.



# Zusammenfassung

Diese Masterarbeit untersucht das Konzept von 'Crackling' in nanoporösen Materialien (im Speziellen Gelsil und Vycor, beides  $\text{SiO}_2$ -basierte synthetische Materialien).

'Crackling' bezieht sich hier auf eine ruckartige Antwort eines Systems auf eine veränderliche äußere Bedingung, wie eine antreibende Kraft. Die Störung des Systems durch die äußere Kraft resultiert in ruckartigen Ereignissen (Lawinen) in einer Vielzahl von Größen. Solche 'Crackling'-Ereignisse können in verschiedenen Systemen auftreten, vom Zerknüllen von Papierstücken bis hin zu Erdbeben. Aktuelle Arbeiten zeigen, dass vielen dieser Systeme, in denen solch ruckartige Ereignisse auftauchen, ähnliche Potenzgesetze zugrunde liegen [26].

Im Fall von porösen Materialien kann 'Crackling' beobachtet werden, wenn das Material zusammengepresst wird und Lawinen, durch korreliertes Brechen von nanometergroßen Poren, auftreten. Dadurch verformt sich die Probe nicht gleichmäßig sondern in kleinen Sprüngen. Neue Studien (z.B. [4], [27], [23]) an porösen Materialien haben gezeigt, dass dieses Verhalten analysiert werden kann, indem auf eine Probe eine Druckspannung ausgeübt wird und gleichzeitig die Schallemission gemessen wird.

Die Hauptaufgabe während dieser Arbeit war es eine neue Methode für die Untersuchung von 'Crackling' in porösen Materialien zu analysieren [30]. Diese neue Methode beinhaltet Experimente mit einem dynamischen mechanischen Analysator, mit welchem sowohl die Druckkraft auf die Probe langsam in Raten von etwa  $0.1\text{mN/s} - 10\text{mN/s}$  aufgebracht wurde, als auch die Veränderungen der Probenhöhe gemessen wurden. Tatsächlich wurden ähnliche Potenzgesetze der 'Crackling'-Ereignisse wie in Schallemissionsexperimenten gefunden, deren Exponenten auch mit den berechneten Werten der Molekularfeldtheorie übereinstimmen.



# Sabine Puchberger

*Curriculum Vitae*

## PERSONAL DETAILS

---

*Name* Sabine Friedericke Puchberger, BSc  
*Birth* March 24, 1991  
*Birthplace* Waidhofen an der Ybbs  
*Nationality* Austria

## EDUCATION

---

### Master studies in Physics

*University of Vienna*

Oct. 2014 -  
present

### Bachelor studies in Physics

*University of Vienna*

Oct. 2011 -  
July 2014

### Studies in English/Spanish

*University of Vienna*

Oct. 2010 -  
July 2011

### Commercial Highschool

*Waidhofen/Ybbs*

Sept. 2005 -  
June 2010

### Secondary School

*Waidhofen/Ybbs*

Sept. 2001 -  
July 2005

### Primary School

*Waidhofen/Ybbs*

Sept. 1997 -  
July 2001